Experimental Cardiovascular Imaging (ExCaVI)

Core Facility Small Animal Imaging

Head: Prof. Dr.rer. nat. Volker Rasche

Department of Internal Medicine II

University of Ulm

Real-time Cardiac MRI in the Mouse Model

Dissertation applying for

Doctor Degree of Medicine (Dr. Med.)

Faculty of Medicine, University of Ulm

Submitted by

Hao Li

Born in Shen'xian P. R. China

2019

Amtierender Dekan: Prof. Dr. rer. nat. Thomas Wirth

1. Berichterstatter: Prof. Dr. rer. nat. Volker Rasche

2. Berichterstatter: Prof. Dr. med. Meinrad Beer

Tag der Promotion: 22-10-2020

Parts of this dissertation have already been published in the following journal articles:

Li H, Metze P, Abaei A, Rottbauer W, Just S, Lu Q, Rasche V. Feasibility of real-time cardiac MRI in mice using tiny golden angle radial sparse. NMR Biomed. 2020 Mar 29:e4300. doi: 10.1002/nbm.4300. Distributed under CC BY-NC, https://creativecommons.org/licenses/by-nc/4.0/

Li H, Abaei A, Metze P, Just S, Lu Q and Rasche V (2020) Technical Aspects of in vivo Small Animal CMR Imaging. Front. Phys. 8:183. doi: 10.3389/fphy.2020.00183. Distributed under CC BY 4.0, https://creativecommons.org/licenses/by/4.0/

Contents

Abbreviations

ASL	Arterial spin labeling
B_0	Static magnetic field
BSA	body surface area
Bpm	Beats per minute
b-SSFP	Balanced steady-state free precession
CI	cardiac index
CMR	Cardiovascular magnetic resonance
CNR	Contrast-to noise ratio
CNR	Contrast-to noise ratio
CO	Cardiac output
CoV	Coefficient of variation
Cpm	Cycles per minute
DCM	Dilated cardiomyopathy
DTPA	Diethylene triaminepentaacetic acid
EDV	End-diastolic volume
EF	Ejection fraction
ESV	End-systolic volume
FFT	Fast Fourier Transform
FLASH	Fast low-angle shot
GA	Golden angle
Gd	Gadolinium
GRE	Gradient echo
GRAPPA	Generalized autocalibrating partially parallel acquisitions
Heterozygous	Het
HR	Heart rate
IG	Self-gated sequence
LV	Left ventricle
LVMED	Left ventricle mass at end diastole
LVMES	Left ventricle mass at end systole
MRI	Magnetic resonance imaging
Nexilin Knock-out	Nexn KO
NMR	Nuclear magnetic resonance
RF	Radiofrequency
ROI	Region of interest
RT	Real time
SAX	Short axes orientations
SC	Compressed sensing
SD	Standard deviation
Semi-2CH	Semi-two-chamber
Semi-4CH	Semi-four-chamber
SI	Signal intensity
SNR	Signal-to noise ratio
SV	Stroke volume
TE	Echo time

TM	Transverse magnetization
TR	Repetition time
tyGA	Tiny golden angle
tyGRASP	Tiny golden angle radial sparse
Wild-type	WT

1 Introduction

1.1 Cardiac magnetic resonance imaging

1.1.1 Introduction to magnetic resonance imaging

Magnetic resonance imaging (MRI) is a tremendously versatile and flexible imaging modality, providing high resolution images in any arbitrary plane without the risk of ionizing radiation. It is founded on the basic physics of nuclear magnetic resonance (NMR), which was first experimentally certified by Purcell et al.(Purcell et al., 1946) and Bloch(Bloch, 1946) in 1946. A MRI system mainly contain three electromagnetic components: the main magnet coils to provide powerful static magnetic field (B_0), three gradient coils to create linear slopes in field strength in any direction, and an integral radio-frequency (RF) transmitter coil to generate and transmit pulses of electromagnetic radiation(Currie et al., 2013; Ridgway, 2010).

The MRI signal is mainly generated by ^1H protons in the body, mostly in water molecules. After polarized by the strong B_0, the spins of the protons align with B_0. The application of RF excitation pulse produces transverse magnetization (TM), which can be measured by a receive coil(Plewes and Kucharczyk, 2012). MR systems encode spatial information in the MR signal with the gradient system. All data are measured in k-space, and the image is reconstructed by an inverse fast Fourier transform (FFT)(Gallagher et al., 2008).

In the past two decades MRI has been established as a valuable tool for studying cardiovascular disease. Cardiovascular magnetic resonance (CMR) imaging has proven to be an accurate technique in the detection and characterization of structural and functional cardiac abnormalities. Especially its versatility, accuracy and high reproducibility has made CMR the non-invasive reference modality for deriving global and regional myocardial function, quantification of fibrotic myocardium and more advanced tissue characterization in clinical and preclinical diagnosis(Li et al., 2020a; Messroghli et al., 2017; Petersen et al., 2017; Peterzan et al., 2016; Schneider et al., 2003).

1.1.2 Self-gated FLASH cine sequence

MRI is an essential medical imaging tool with an inherently slow data acquisition process. The invention of fast low-angle shot (FLASH) gradient echo MRI in 1985(Haase et al., 1986) with its about 100-fold reduction of acquisition time

broadened the application of MRI examinations and enables dynamic cardiac imaging. However, CMR imaging generally requires synchronization of the data acquisition to the cardiac and respiratory motion. In conventional CMR imaging, the electrocardiogram (ECG) signals are applied for synchronization(Rose et al., 1994). But the complexity with ECG gating and the distortion of ECG signal (Fig.1) by the switched gradient fields limit its application.

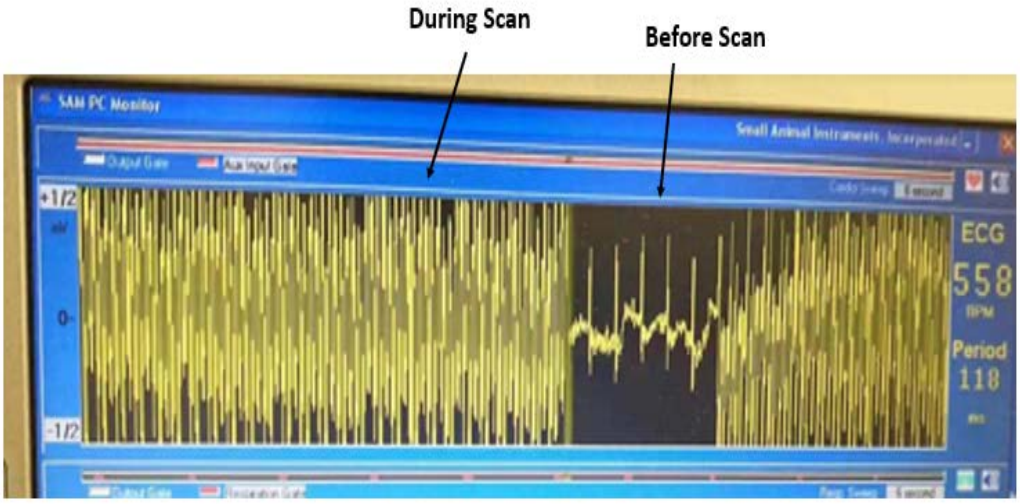

Figure 1: After acquisition, the ECG signal is distorted by the switched gradient fields.

To reduce the motion artifacts of respiration, cardiac triggering has also to be combined with respiratory gating. Hiba et al.(Hiba et al., 2006) developed cardiac and respiratory double self-gated FLASH cine sequence to achieve high quality cine-MRI in small animal hearts.

More recently, retrospectively triggered protocols not using a physiological signal for data synchronization have been introduced(Fries et al., 2012). Here an additional navigator signal is acquired prior to each echo. After the scan, this navigator signal is analyzed and used to assign each echo to its correct position in the cardiac and respiratory cycles.

Over the last years, self-gating techniques have been introduced enabling high-quality cardiac MRI with high reproducibility(Joubert et al., 2017; Vanhoutte et al., 2015; Zuo et al., 2017). However, the acquisition times in the minute range for a single slice still limit its application for pharmacological stress or first-pass perfusion imaging.

1.1.3 Real-time CMR

Real-time imaging refers to the rapid and continuous acquisition of image datasets followed by image reconstruction and visualization. To reduce acquisition times, dedicated real-time methods for the rapid and continuous acquisition of image datasets, such as parallel imaging(Breuer et al., 2005; Griswold et al., 2002; Seiberlich et al., 2011), k-t acceleration methods(Bollache et al., 2018; Feng et al., 2013; Schnell et al., 2014), and compressed sensing (CS)(Kido et al., 2016; Lustig et al., 2007; Otazo et al., 2010), have been suggested and initially evaluated(Wech et al., 2016). As the MRI data are redundant, acceleration can be achieved by undersampling, thus reducing the amount of acquired data for a single frame of an image series. Iterative reconstruction algorithms ensure image fidelity, e.g. by adding spatial and temporal regularization. Recent progress in real-time MRI result in high quality images with high signal-to-noise ratio (SNR), adequate spatial resolution and unsurpassed temporal resolution(Frahm et al., 2019; Uecker et al., 2010; Xue et al., 2013; Zhang et al., 2010).

1.1.3.1 Spoiled gradient echo sequences

Spoiled gradient echo (GRE) pulse sequences (known by the commercial names of FLASH, T1-FFE, SPGR) are fast MRI techniques based on rapid gradient-echo acquisitions. With a very short repetition time (TR), it can supply a more complex contrast property(Chavhan et al., 2008). The TR values are much shorter than T2 relaxation times of the tissue, then there is not enough time for transverse magnetization to fully decay before applying next RF pulse, and there will be residual transverse magnetization left over. This can potentially contribute to the signal in the subsequent TR periods(Ridgway, 2010). In the spoiled GRE sequences, after the signal is acquired with reversal of the readout gradient, residual TM is de-phased with a spoiler gradient at the end of each TR period so that its contribution to subsequent TR periods is suppressed(Zur et al., 1991).

With advances in MRI system, ultra-high magnetic fields are applied in animal research to supply high quality images. Due to the property, spoiled GRE sequences are widely used for anatomic functional cardiac imaging and for the assessment of myocardial viability in animal imaging under ultra-high magnetic fields. The application of a low flip angle allows much shorter TR, but still larger TM by following low flip angle pulses(Frahm et al., 1986; van der Meulen et al., 1985). Then good SNR, contrast to noise ratio (CNR) and increased speed of acquisition can be achieved by properly

combing TR, TE and flip angle.

Even though this technique yields high quality images, it still suffers from arrhythmia and respiration synchronization. And in order to further satisfy the highly required accelerate acquisition for animal imaging, we combine the spoiled GRE sequences with radial trajectory. The direction of the readout gradient is rotated in a series of projections like the spokes of a wheel(Finn et al., 2006).

By combining the radial acquisition with optimized projection order and dedicated reconstruction techniques, we could achieve a temporal resolution less than 20ms in cardiac animal imaging.

1.1.3.2 Radial trajectory

During the acquisitions, MR data is continuously acquired to construct a single image. In each acquisition, an RF excitation pulse gives energy to the hydrogen nuclei, creating magnetization in the transverse plane, which is then sampled along a particular trajectory in k-space. Traditionally the k-space sampling pattern is designed to meet the Nyquist criterion, which depends on the resolution and field of view. It states that when digitizing a signal containing several frequencies, the highest frequency present in the modulation must be sampled at least twice to accurate digitization.

Since now, the most popular trajectory uses straight lines from a Cartesian sampling pattern, which fills k-space line by line. The principle advantage of Cartesian sampling is that the data elements are regularly spaced and can be efficiently reconstructed by FFT. Compared with Cartesian sampling, with the radial trajectory, k-space is sampled with a set of radial profiles each covering the center of k-space(Wundrak et al., 2015). The radial spokes rely on frequency-encoding gradients and make equal contributions to the images. The radial acquisitions are less susceptible to motion artifacts. Further, due to the continuous recording of all spatial frequencies with every single spoke, undersampling results in almost incoherent artifacts, often showing no noticeable effect on the reconstructed images(Uecker et al., 2012).

Winkelmann et al.(Winkelmann et al., 2007) showed that a uniform profile distribution is guaranteed with a constant golden angle (111.246°) increment for a fixed number of profiles. The concept of Golden Angle (GA) angular spacing enabled data acquisition with optimal k-space coverage almost independent on the number of projections (Fibonacci sequence) and ensured incoherent undersampling artifacts(Wech et al., 2016). However, the large angular increment of the golden angle profile order leads to

an abruptly changing gradient scheme, which leads to rapidly changing eddy currents in the conducting part of the magnet, resulting in a rapidly varying field inhomogeneities. The steady state of b-SSFP sequence is prone to the varying eddy current effects and may exhibit strong signal fluctuations(Wundrak et al., 2015). Its extension to tiny golden angle (tyGA)(Wundrak et al., 2016) enabled the translation of the GA principle to higher field strength and provided even larger flexibility in the selection of the number of projections used for reconstruction of a single frame (generalized Fibonacci sequence, Fig.2), but without rapid gradient changes.

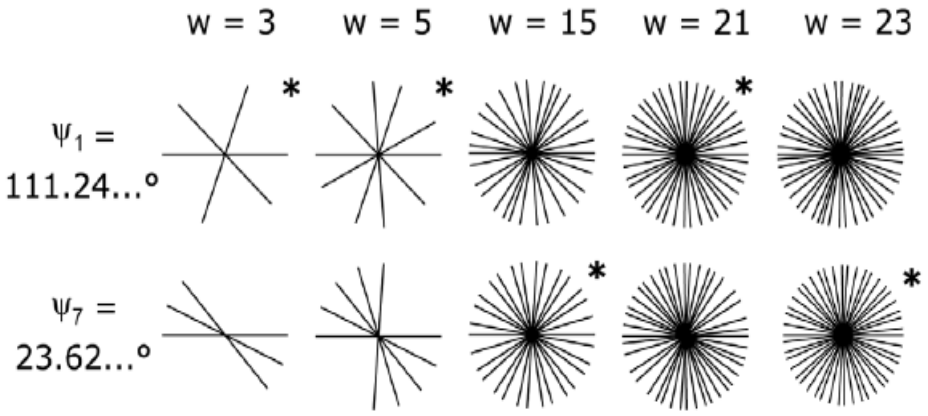

Figure 2: Golden angle ordering $\boldsymbol{\psi}_1$ compared to tiny golden angle ordering $\boldsymbol{\psi}_7$. Both exhibit a near optimal radial profile distribution if w >2*N*, especially if w is an element of the generalized Fibonacci sequence G^N (marked with *). With kind permission of (Wundrak et al., 2016).

1.1.3.3 Compressed sensing

Compressed sensing (CS) was firstly introduced by Donoho and Candès in 2004(Candes et al., 2006; Donoho, 2006). They have developed its mathematic foundation. Later it was translated to MRI by Lustig et al.(Lustig et al., 2007). CS aims to reconstruct signals and images from a reduced number of k-space samples not following Nyquist criterion. As the MRI data are redundant and naturally compressible by sparse coding in some appropriate transform domain, CS has the potential to significantly reduce scan time.

A successful application of CS has three basic requirements(Lustig et al., 2008): (1) the desired images have a sparse representation in a known transform domain, (2) incoherence of the undersampling artifacts, (3) use of a nonlinear reconstruction algorithm that enforces sparsity constrained by data consistency.

1.1.3.3.1 Sparsity

Most MR images are sparse in an appropriate transform domain, and they can be characterized by only a small number of non-zero coefficients (Fig.3). For the transform-based compression, a sparsifying transform is applied at first, and the mapping image content into a vector of sparse coefficients, then it only encodes the non-zero or most significant coefficients and ignores the smaller coefficients. With a mathematical transformation (data compression), we can produce a sparse representation of the images. In order to achieve maximal acceleration, a high degree of sparsity is desired. Such as the dynamic cardiac MR images, the quasi-periodicity of cardiac images has a sparse temporal Fourier transform, so they are highly compressible. This enables higher acceleration for dynamic imaging than static imaging(Feng et al., 2017).

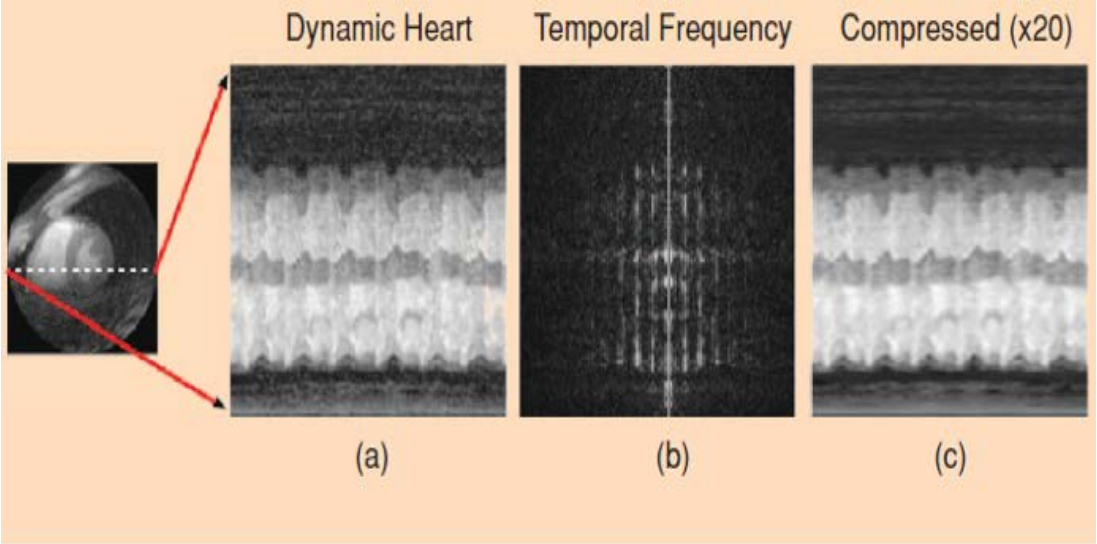

Figure 3: Transform sparsity of MR images. **(a)** Fully sampled images have sparse representations in an appropriate **(b)** transform domain. Only a small number of high-value coefficients are preserved while all others are set to zero; the transform is inverted forming a **(c)** reconstructed image. With kind permission of (Lustig et al., 2008).

1.1.3.3.2 Incoherence of the undersampling artifacts

The artifacts in reconstruction caused by undersampling should be incoherent, i.e. that they must manifest as noise like patterns in the sparse domain. (Fig.4a). However, irregular undersampling patterns lead to aliasing artifacts that looks like noise and often do not obscure the image, known as incoherent aliasing artifacts. Various undersampling strategies have been proposed to meet the incoherence requirement. In the Cartesian sampling, some k-space lines can be pseudo-randomly omitted, resulting in more incoherent artifacts (Fig.4b). Alternatively, due to its highly incoherent undersampling property, many non-Cartesian trajectories, such as radial trajectories (Fig.4c), are widely used in CS applications. Especially when the radial trajectories are designed with angular rotation of subsequently measurements by the golden angle, which ensures nearly uniform k-space coverage for many useful subsets of acquired data. This approach enables continuous data acquisition and flexible number of projections for retrospective image reconstruction for the dynamic cardiac imaging.

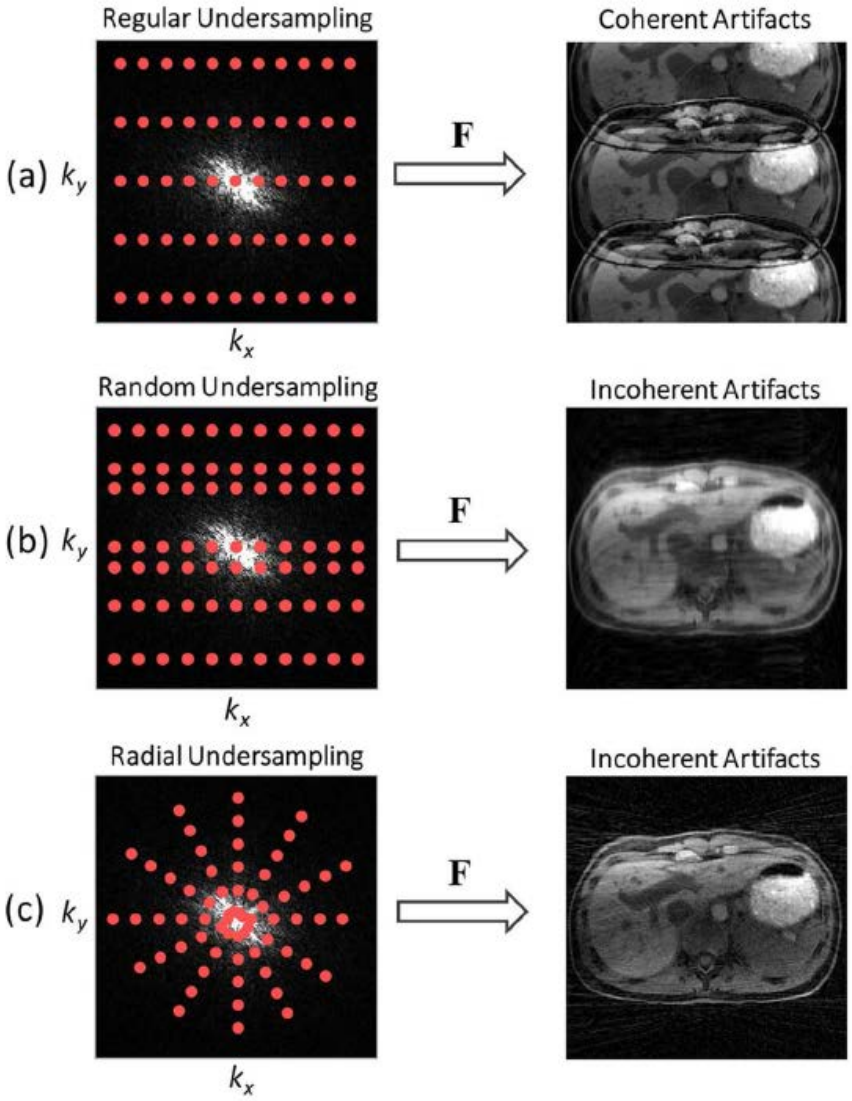

Figure 4: a: Regular undersampling results in coherent aliasing of the signal structure; **b:** Random undersdampling lead to incoherent artifacts that appear like added noise; **c:** radial sampling permits undersampling along both spatial dimension and thus enables a higher level of incoherence. With kind permission of(Feng et al., 2017).

1.1.3.3.3 Image Reconstruction

If the requirements of a sparsity and incoherent aliasing artifacts are achieved, a CS iteratively reconstruction algorithm can be applied to suppress the incoherent aliasing artifacts. In our case, we applied a compressed sense reconstruction with total variation sparsity operator along the spatial and temporal domain according to

argmin $\|\boldsymbol{F}\cdot\mathbf{S}\cdot\boldsymbol{x}-\boldsymbol{b}\|_2^2+\boldsymbol{\lambda_t}\|\boldsymbol{\nabla_t x}\|_1+\boldsymbol{\lambda_s}\|\boldsymbol{\nabla_s x}\|_1$ (Wundrak et al., 2016).

The details are explained in the method part.

1.2 CMR in Mouse Model

1.2.1 Mouse models of heart disease

Cardiovascular disease is considered as the first leading cause of death in the developed world, with high morbidity and mortality. In preclinical research, small rodent animal models of human cardiovascular disease are frequently used to investigate the basic underlying mechanism of normal and abnormal cardiac function and for monitoring the disease progression under therapy(Camacho et al.). Over the past decades, with the experimental animal models (especially mouse models), enormous achievements have been made in cardiac disease. Because mice are easier to handle and house, have a short gestation time, high breeding rate and short life span, they allow researchers to follow the development process of the disease at an accelerated way. Further, due to their short gestation time of 18-21 days and short life span, transgenic mouse models can be efficiently developed(Milani-Nejad and Janssen, 2014).

Nowadays, translational research accounts for a large proportion of animal studies operated every year. Since the implementation of the 3 Rs principles (replacement, refinement, reduction) into the European Directive 2010/63/EU, medical imaging is highly recommended in translational research, because it can visualize the disease from the beginning in a real time, quantitative and non-invasive way. It has potential to significantly reduce the number of experimental animals and animal welfare is highly concerned. Due to the high spatial and temporal resolution and multiple properties, MRI has been proven to be a great diagnostic imaging tool in small animal models to monitor disease progression and response to treatment. However, the small size of the mouse heart (5-6mm left ventricle (LV) diameter, approximately 0.2g of heart weight)(Wessels and Sedmera, 2003), high heart rates (about 250-600 beats per minute [bpm]), high respiratory rates (about 60-160 cycles per minute [cpm]), and fast systemic blood circulation time (4-5 heart beats) impose substantial challenges for functional assessment by MRI. Rapid data acquisition strategies for functional MRI with high temporal resolution, while preserving adequate spatial resolution, and sufficient volumetric coverage are required.

1.2.2 Nexilin induced DCM model

Dilated cardiomyopathy (DCM) represents a serious cardiac disorder defined by dilation and impaired systolic function of the left or both ventricles, in the absence of coronary artery disease, valvular abnormalities, or pericardial disease(Schultheiss et al., 2019). DCM causes heart failure, serious arrhythmias, thromboembolic events, which cause a poor quality of life and a reduced life expectancy.

Genetic mutations have been proven as one of the main causes of DCM. So far, over hundreds of mutations in more than 30 genes associated with DCM have been identified. The majority of genetic DCM is inherited in an autosomal-dominant manner, but it can be also transmitted as an autosomal recessive, X-linked and mitochondrial trait(McNally and Mestroni, 2018). Genetic studies reveals that contractile dysfunction of myofibrils plays an important role in initiation and progression of DCM, and the mutations in genes encoding sarcomere proteins, cardiac troponins, phospholamban, desmosomal proteins are associated with DCM(Schultheiss et al., 2019).

Recently, David et al.(Hassel et al., 2009) found multiple mutations in the nexilin (Nexn) gene are associated with DCM in humans, and deficiency of Nexn in zebrafish results in perturbed Z-disk stability and heart failure. The z-discs are the lateral boundary of the sarcomere, connecting the filamentous F-actin, titin, and nebulin/ nebulette, and also play an important role as nodal point in cardiomyocyte signal transduction(Frank and Frey, 2011). Later, Aherrahrou et al.(Aherrahrou et al., 2016) translated the deficiency of Nexn gene in mice model, which leads to rapidly progressive DCM and reported endomyocardial fibroelastosis, resulting in premature death in perinatal period. Liu et al.(Liu et al., 2019) found Nexn interacts with sarcoplasmic reticulum proteins, and it is a pivotal component of junctional membrane complexes required for initiation and formation of cardiac T-Tubules. These functional analyses using zebrafish and mouse models demonstrated a key role for Nexn in ventricular dilation resulting in DCM induced severe heart failure.

1.2.3 Functional imaging

The heart can be considered as a central circulatory pump, generating the driving force to propagate the blood though the vascular system. Visualization and quantification of the cardiac function are crucial, as many diseases have an impact on the performance of the heart.

Global ventricular performance parameters (Table 1) are widely used in clinic or preclinic research to evaluate cardiac function, which means the capability of the ventricles to eject blood into the great vessels. For the accurate volumetric quantification, the Simpson's rule is applied, based on a stack of parallel slices entirely covering the whole ventricle.

Table 1: Global functional parameters. *EDV* end-diastolic volume, *ESV* end-systolic volume, *SV* stroke volume, *EF* ejection fraction, *HR* heart rate, *CO* cardiac output, *BSA* body surface area, *CI* cardiac index.

EDV- ESV = SV (ml)
SV/EDV = EF (%)
SV x HR= CO (ml/min)
EDV_{index} = EDV/BSA (ml/m^2)
ESV_{index} = ESV/BSA (ml/m^2)
CO/BSA = CI ($ml/min/m^2$)

Since the first publications on the use of MRI for quantification of cardiac function(Longmore et al., 1985), MRI is gradually used to validate other quantification approaches, indicating that MRI is the reference method for accurate assessment of cardiac function(Nesser et al., 2009; Niemann et al., 2007; Sugeng et al., 2006).

One of the promising application for real-time MRI is cardiovascular imaging(Brinegar et al., 2008; Wech et al., 2016; Zhang et al., 2010). Compare with standard ECG-triggered cine imaging, which rely on ECG-synchronized acquisitions and acquire data from multiple cardiac cycles, the real-time CMR imaging has various advantages. As the real-time imaging is sufficiently fast enough to freeze motion, cardiac and respiratory synchronization is not required any more. And the rapid and continuous acquisition of image data can further shorten the scan time. In case of GA acquisition, the following reconstruction allows image series with different temporal resolution. However, the reduced spatial resolution in real-time imaging would results in impaired image quality, which maybe affect the accuracy of diagnosis. So further optimize implementations are highly required for real-time imaging.

1.2.4 Pharmacological stress imaging

Assessment of the left ventricular function under pharmacological stress is widely used in cardiovascular patients to detect myocardial viability, ischemia or cardiac reserve and to determine the risk of subsequent cardiovascular event. However, due to the fast half-time and rapid metabolism of special drugs, a sufficiently technique is highly required by biologists and geneticists to visualize acute changes of cardiac geometry and function during pharmacological stress in the preclinical research.

Vasodilator and dobutamine are the main pharmacological agents used in stress CMR imaging(Le et al., 2017). By activating adenosine receptors, vasodilators agents can trigger coronary vasodilation and directly increase coronary flow(Saab and Hage, 2017). Dobutamine is a synthetic catecholamine that primarily stimulate β_1-adrenergic receptor and mildly stimulate α_1, β_2-adrenergic receptor, and augments myocardial contractility(Charoenpanichkit and Hundley, 2010). Since Wiesmann et al.(Wiesmann et al., 2001) firstly use the dobutamine stress MRI to reveal the loss of inotropic and lusitropic response in mice with myocardial infarction and diastolic dysfunction as an early sign of cardiac dysfunction in a transgenic mouse model of heart failure, more and more studies using the dobutamine stress MRI to investigate cardiac function in mouse model(Palmer et al., 2017; Stuckey et al., 2012; Tyrankiewicz et al., 2013). Different dobutamine doses and ways of administration were used in these studies (4 or 40 ug/minute/kg, intravenous infusion [i.v.] or 1.5ug/g body weight, intra-peritoneal bolus injection [i.p.]).

In our study, we selected the most frequently used dose in previous studies (1.5ug/g body weight i.p.)(Wiesmann et al., 2001). The real-time technique combined with high field MRI used in this work allowed us to non-invasively characterize the acute changes of murine cardiac function from baseline to physiologically stressed conditions in vivo without ECG and respiration synchronization, and enables flexible numbers of projections for image reconstruction to achieve high spatial and temporal resolution.

1.2.5 First-pass perfusion imaging

Assessment of myocardial perfusion is considered to be a key parameter in the characterization of cardiac pathology and evaluation of patient outcomes, especially ischemic heart disease or microvascular dysfunction. In normal circumstances myocardial oxygen supply is balanced to the continuous changing myocardial oxygen demand. The imbalance of supply and consumption may result in myocardial ischemia. In a clinical setting, perfusion MRI and late-gadolinium enhancement MRI are widely used for evaluation of the myocardial perfusion status(Hernandez, 2018; Sun et al., 2018; Vincenti et al., 2017). Parallel to progress in perfusion imaging in humans, translation of time efficient and reproducible quantitative myocardial perfusion method into animal models is highly desired. Currently, myocardial perfusion in rodents is typically estimated using arterial spin labeling (ASL)(Kober et al., 2005, 2016; Streif et al., 2005) and first-pass perfusion imaging(Coolen et al., 2010; van Nierop et al., 2013). However, the ASL suffers from relatively long acquisition times and it is prone to variations in both heart and respiratory rates(Kwiatkowski and Kozerke, 2019). The basic principle of first-pass perfusion imaging involves intravenous injection of a bolus of a suitable contrast agent, after which the first pass of the contrast agent through the heart is monitored.

MR contrast agents work by modifying the tissue properties that most directly affect image contrast appearances. This effect is known as relaxivity and enables better visualization of tissues that are affected by the agent. There are two major classes of MRI contrast agents: those that shorten T1 recovery times are called T1 agents, and those that shorten T2 decay times are called T2 agents. The degree of shortening depends on the concentration of the agent. The most widely used contrast agent is gadolinium (Gd). Gd is highly toxic and could not be excreted by the body and would result in long term side effects as it binds to membranes. By binding the Gd to other molecules such as diethylene triaminepentaacetic acid (DTPA), it could be safely used in most circumstances although Gd-based contrast agents are contraindicated for use in patients with impaired renal function due to their association with nephrogenic systemic fibrosis(Grobner, 2006). Gd is particularly strongly paramagnetic as it has seven unpaired electrons in the outer shell(Biglands et al., 2012). At low concentrations the effect of T1 shortening is dominant, while at higher concentrations the T2 shortening effect becomes the dominant factor.

Due to the high heart rate and fast systemic blood circulation time, a fast imaging

protocol is required for the successfully application of first-pass perfusion imaging in mouse model. In our study, the FLASH sequence is applied to generate higher signal to noise ratio (SNR). The higher SNR of FLASH sequence allows a much higher bandwidth to be selected leading to shorter echo time (TE) and TR, which can further accelerate acquisition. In order to maximise the effect of the contrast agent on signal intensity and cope with arrhythmic cycles, A saturation pulse is applied prior to the read-out pulse sequence. ECG-triggering is applied to ensure the data acquisition for each image slice is performed at the same point in the cardiac cycle in continuous heart beats with one image per cardiac cycle. In this way, the cardiac motion appears frozen when the images are viewed as a dynamic movie, then the quantitative analysis could be conveniently performed.

1.3 The aim of this study

In summary, the aim of this study is to investigate the feasibility of tiny golden angle radial sparse MRI for real-time imaging of cardiac function in the mouse model. Image quality, resulting global functional parameters, and reproducibility are compared between the real-time tyGRASP and the self-gating techniques for different temporal resolutions at 11.7T. As applications potentially benefitting from real-time techniques, dobutamine pharmacological stress and first-pass perfusion imaging are initially investigated.

2 Material and Methods

2.1 Materials

2.1.1 Animals

Nexilin heterozygous mice	Klinik f.IM2 Molekulare Kardiologie, Ulm, Germany
Nexilin wild-type mice	Klinik f.IM2 Molekulare Kardiologie, Ulm, Germany
C57BL/6N mice	Charles river laboratories, Sulzfeld, Germany

2.1.2 Laboratory Equipments

11.7 Tesla small animal MRI system	Bruker BioSpec 117/16, Germany
Four elements thorax coil	RAPID Biomedical, Rimpar, Germany
Isoflurane Vapor 19.3	Drägerwerk AG & Co. KGaA, Lübeck, Germany
Induction chamber	Drägerwerk AG & Co. KGaA, Lübeck, Germany
Infusion pump AL-1000	WPI, USA
Heating blanket	Bruker Biospin GmbH, Ettlingen, Germany
Thermo	Bruker Biospin GmbH, Ettlingen, Germany
Rectal temperature probe	Stony Brook, NY, USA
Balloon pressure sensor	Stony Brook, NY, USA
Small Animal Monitoring & Gating System	Stony Brook, NY, USA
Forceps	Universität Ulm, Ulm, Germany
Scissors	Universität Ulm, Ulm, Germany

2.1.3 Consumable Items

1ml syringe	B|BRAUN, Bad Arolsen, Germany
30G ½ needles	BD Microlance ™ 3, BD Drogheda, Ireland
Heparin	Ratiopharm GmbH, Ulm, Germany
Dobutamine	Fresenius Kabi Deutschland GmbH, Bad Homburg, Germany
Gd-DTPA	Guerbet GmbH, Sulzbach, Germany
Isoflurane	DeltaSelect GmbH, Germany
Normal saline	B|BRAUN, Melsungen, Germany
ECG electrodes	Ambu, Ballerup, Denmark
Bepanthen	Bayer Vital GmbH, Leverkusen, Germany
Tape	BSN medical GmbH, Hamburg, Germany
80% ethanol solution	Universität Ulm-Klinikum Apotheke, Ulm, Germany
0.3x0.6mm Tube	Bohlender GmbH, Grünsfeld, Germany

2.1.4 Analysis Software

ParaVision 5.1	Bruker Biospin GmbH, Ettlingen, Germany
ParaVision 6.01	Bruker Biospin GmbH, Ettlingen, Germany
Matlab	Mathworks, Natick, Massachusetts, USA
Segment	Medviso AB, Lund, Sweden
Prism 7	GraphPad, San Diego, California, USA

2.2 Animals

2.2.1 Ethics approval and consent to participate

Animal experiments were approved by the regional board of Tübingen and conducted according to German law for the welfare of animals and regulations for care and use of laboratory animals. All institutional and national guidelines for the care and use of laboratory animals were followed and approved by the appropriate institutional committees (No. 1221.TSchB: W).

2.2.2 Validation experiments

12 constitutive heterozygous (Het, *N*=6) and wild-type (WT, *N*=6) Nexn KO mice, both groups containing 3 females (20-22g) and 3 males (27-30g) each, were included in this study(Aherrahrou et al., 2016). Further, 3 male healthy wild-type mice (C57BL/6N, 35-37g) were included for the reproducibility assessment. Before the start of the study, the animals were housed in a temperature-controlled environment for at least one week. Facility rooms were maintained at constant temperature (23°C), humidity (50% relative humidity), and 12h light/dark cycle. Access to food and tap water was ad libitum.

2.3 CMR

2.3.1 CMR Image Acquisition

All experiments were performed on an 11.7 Tesla dedicated small animal MRI system (BioSpec 117/16, Bruker Biospin, Ettlingen, Germany). Data were acquired with a four-elements thorax coil (Fig.5, RAPID Biomedical, Rimpar, Germany).

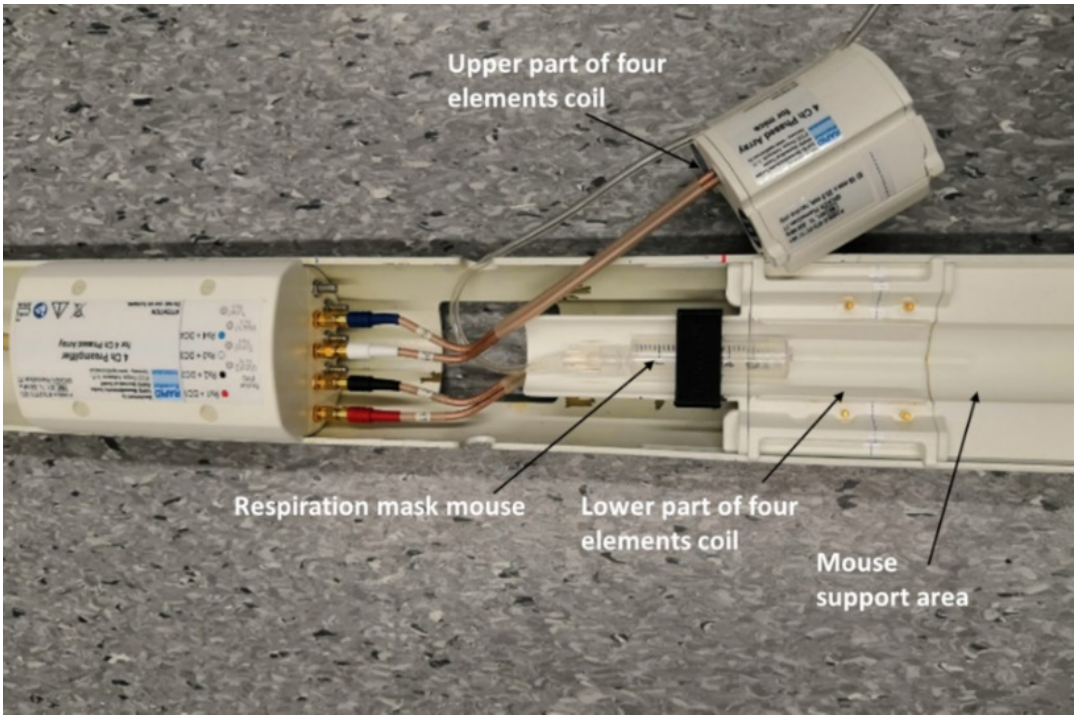

Figure 5: Four-elements thorax coil.

Slice planning was performed as suggested earlier(Zuo et al., 2017) ensuring high reproducibility of the image geometry for subsequent examinations. In short, the imaging protocol comprised a multi-slab survey acquisition in axial, coronal, and sagittal orientation, followed by two long axis CINE scans in semi-two-chamber (semi-2CH) and semi-four-chamber (semi-4CH) geometry. The semi-2/4CH images were used to plan the subsequent stack of short axes orientations (SAX). The number of short axis slices was adjusted to ensure full coverage of the left ventricle in end-diastole (Fig.6). For minimizing TE, in all protocols an asymmetric Sinc-Gauss excitation pulse with 15 kHz excitation bandwidth was used.

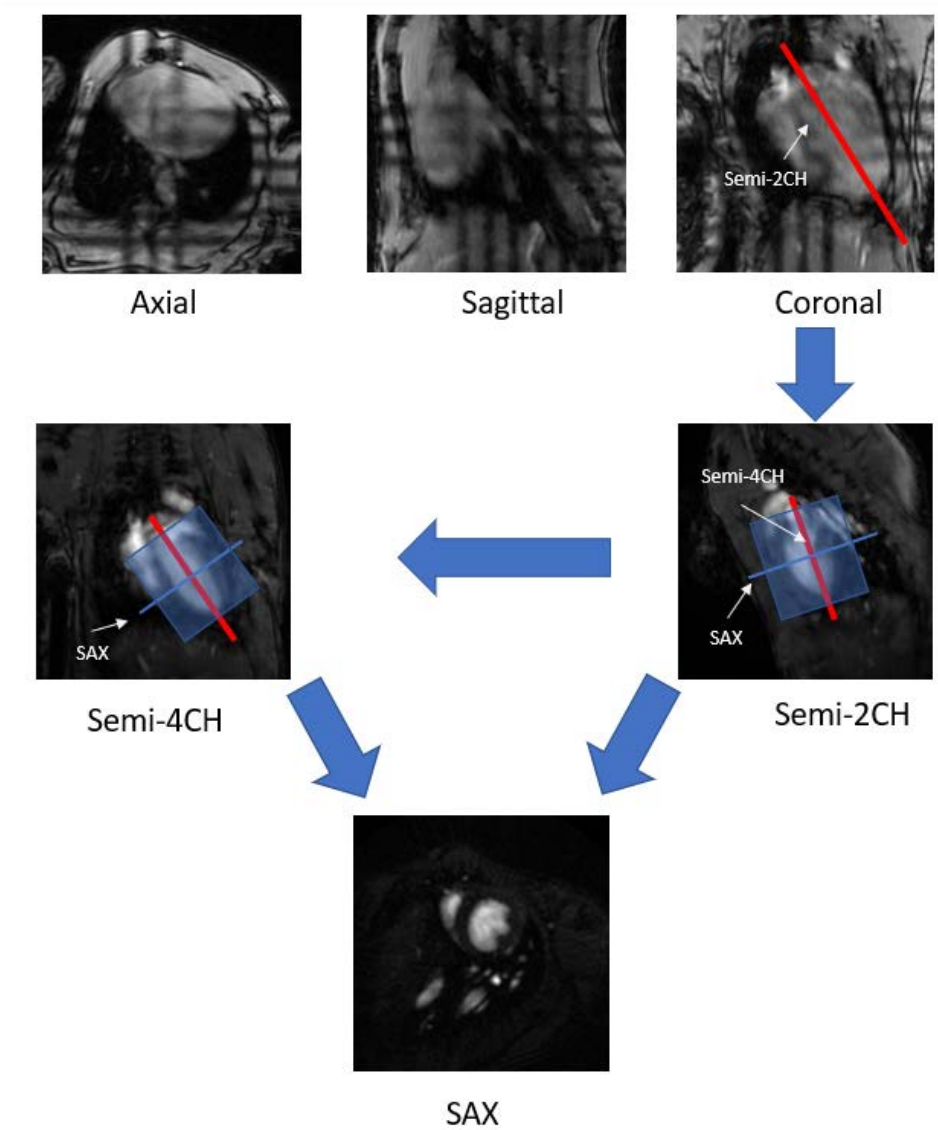

Figure 6: Imaging protocol for highly reproducible imaging of cardiac function and anatomy (2CH: 2 chamber, 4CH: 4 chamber, SAX: short axes orientation).

2.3.2 Gated functional MRI

Reference functional data were acquired applying a conventional Cartesian self-gated sequence (IntraGate©, ParaVision 5.1, Bruker Biospin, Ettlingen,Germany)(Zuo et al., 2017). The principle of the self-gated sequence is shown in Fig.7. The acquisition of each k-space line is modified into two subsequently acquisitions. At the beginning, a navigator signal without phase encoding is generated during the first acquisition, then the subsequent acquisition is encoded from the conventional FLASH technique. Typical imaging parameters were: echo/repetition time TE/TR = 1.0/5.75ms, flip angle $\alpha = 15°$, matrix size = 256x256, in-plane resolution $\Delta r = 0.123^2 \mathrm{mm}^2$, slice thickness $s_D = 0.5\mathrm{mm}$, cardiac frames = 10, bandwidth $bw = 150\mathrm{KHz}$, acquisition time $T_{ACQ} = 42s$ per slice.

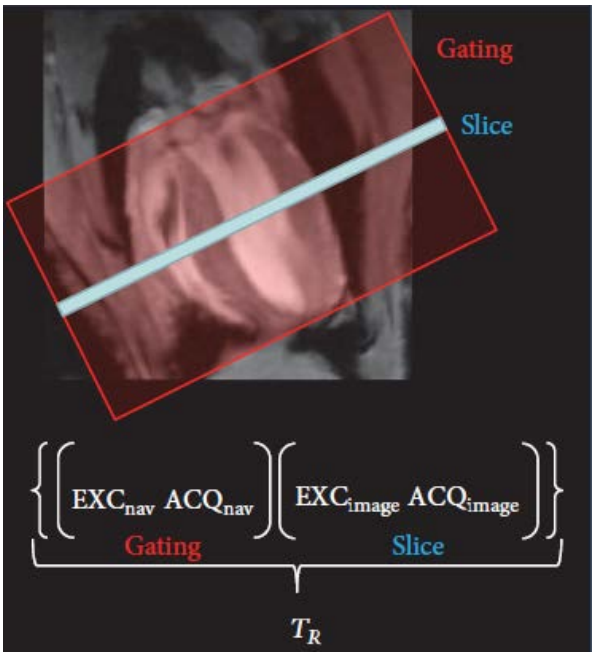

Figure 7: Principle of the self-gated cine imaging protocol. Here an additional navigator signal is acquired prior to each echo. After the scan, this navigator signal is analyzed and used to assign each echo to its correct position in the cardiac and respiratory cycles. With kind permission of (Zuo et al., 2017).

2.3.3 Real-time functional MRI

A tiny golden angle radial trajectory as suggested by Wundrak et al.(Wundrak et al., 2016) was implemented on the small animal system (ParaVision 6.01, Bruker Biospin, Ettlingen,Germany). For real-time imaging, spatial resolution was slightly compromised with the MR acquisition parameters as: TE/TR = 0.86/2.1ms, flip angle $\alpha = 20°$, matrix size = 150x150, in-plane resolution $\Delta r = 0.2^2\text{mm}^2$, slice thickness $s_D = 1\text{mm}$, $bw = 250\text{KHz}$, $T_{ACQ} = 1.2s$ per slice. A tiny GA of $\varphi_7 = 23.62814°$ was used providing homogenous k-space coverage with $G_3^7 = 8$ (RT1), $G_4^7 = 15$(RT2), and $G_5^7 = 23$ (RT3) projections, yielding temporal resolutions of $\Delta t = 16.8, 31.5, \text{and } 48.3\text{ms}$ (Fig.8).

Prior to each tyGA acquisition, the actual trajectory was mapped independently for all gradient directions as suggested by Zhang et al.(Zhang et al., 1998) and calculated for the respective image geometry.

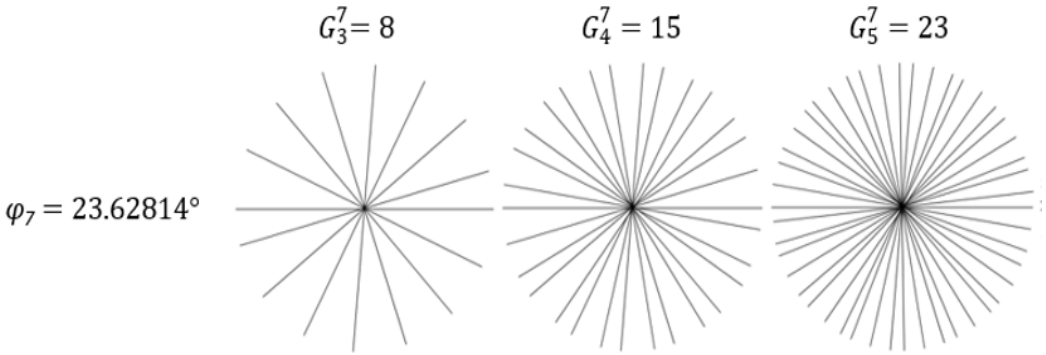

Figure 8: Tiny golden angle radial k-space. A tiny golden angle of $\varphi_7 = 23.62814°$ was used providing homogenous k-space coverage with $G_3^7 = 8$ (RT1), $G_4^7 = 15$(RT2), and $G_5^7 = 23$ (RT3) projections, yielding temporal resolutions of $\Delta t = 16.8, 31.5, \text{and } 48.3\text{ms}$. (Li et al., 2020b), CC BY-NC 4.0, https://creativecommons.org/licenses/by-nc/4.0/

2.3.4 First-pass perfusion Imaging

For first pass perfusion assessment, the continuous tyGA sequence was combined with block-wise cardiac synchronization(Li et al., 2020b) (Fig.9).

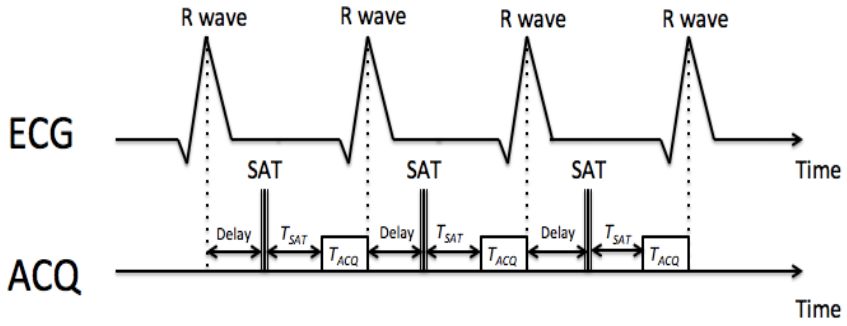

Figure 9: First-pass perfusion sequence: The tyGA (tiny golden angle) acquisition is split into the subsequent acquisition of individual blocks ($G_4^7 = 15$, T_{ACQ} = 31.5ms), the acquisition of which is synchronized with the ECG. Background suppression and coping with arrhythmic cycles are achieved by additional non-selective saturation. (Li et al., 2020b), CC BY-NC 4.0, https://creativecommons.org/licenses/by-nc/4.0/

During each cardiac cycle, a single block of $G_4^7 = 15$ projections with acquisition duration of $\Delta t = 31.5\text{ms}$ was acquired. For suppression of the background signal and coping with arrhythmic cycles, a non-selective saturation pulse was additionally applied prior to each acquisition block with a saturation recovery time T_{SAT} of 60 ms. The trigger delay was chosen such that the acquisition was performed during end-diastole to further minimize motion artifacts (Fig.10).

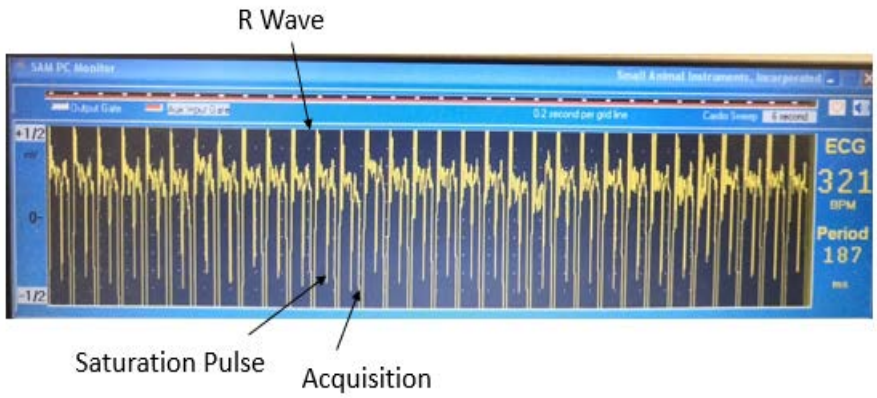

Figure 10: ECG signal during scan. According to the heart rate, a trigger delay was set after the detection of R wave, then the blood and myocardial signal were approximately nulled by a non-selective saturation pulse. The acquisition was performed during the end-diastole.

2.3.5 Data reconstruction

All gated functional MR data were reconstructed by the IntraGate© reconstruction software provided by the vendor. The tyGA data were reconstructed with an in-house developed reconstruction framework, implemented in Matlab (Matlab, The MathWorks, Natick, Massachusetts, USA), applying a compressed sense reconstruction with total variation sparsity operator along the spatial and temporal domain according to

argmin $\|F \cdot \mathrm{S} \cdot x - b\|_2^2 + \lambda_t \|\nabla_t x\|_1 + \lambda_s \|\nabla_s x\|_1$ (Wundrak et al., 2016),

with $\hat{F}$ being the nonuniform Fourier transformation between Cartesian $x - t$ to radial $k - t$ space and S contains the coil sensitivity maps for all coils. The l_2-norm enforces data consistency between $k - t$ space samples *b* and the reconstructed image sequence *x* in $x - t$ space. $\nabla_s \; and \; \nabla_t$ denote the gradient operator along the spatial and temporal dimension. In all cases 50 iterations were used and the strength of the spatial λ_s and temporal λ_t regularization were fixed to $\lambda_s = 0.05$ and $\lambda_t = 0.005$.

2.4 In Vivo Measurements

All mice were anesthetized with isoflurane (5% for induction, 1-1.5% for maintenance, to maintain the respiratory frequency between 60-80 respiratory cycles per minute) in medical air (0.1L/min). During scanning, the respiratory rate was monitored with a balloon pressure sensor and the temperature of the mice was maintained by a water heating blanket.

2.4.1 Assessment of LV function

The gated and real-time imaging protocols were performed in 12 constitutive Nexn KO mice, Het (*N*=6) and WT (*N*=6), for a short axis stack completely covering the left ventricle. End-diastolic volume (EDV), end-systolic volume (ESV), stroke volume (SV), ejection fraction (EF), left ventricle mass at end-diastole (LVMED) and end-systole (LVMES) were quantified with Segment(Heiberg et al., 2010) (Medviso AB, Lund, Sweden) and compared between the real-time and self-gated (IG) acquisition protocols.

2.4.2 Dobutamine stress MRI

For assessment of the performance of the real-time techniques under pharmacological stress, the Nexn mice were additionally scanned after intra-peritoneal injection of 1.5µg/g body weight dobutamine(Tyrankiewicz et al., 2013; Wiesmann et al., 2001). LV functional parameters (EDV, ESV, SV, EF), and cardiac output (CO) were compared between $G_3^7 = 8$ (RT1), $G_4^7 = 15$ (RT2), and $G_5^7 = 23$ (RT3) protocols.

2.4.3 First-pass perfusion MRI

One week after dobutamine stress imaging, Nexn mice were additionally scanned for assessment of the feasibility of first-pass perfusion imaging with the tyGRASP technique. Data acquisition was performed in a mid-ventricular slice. ECG was recorded from two electrodes placed at the right front and left hind paws. A home-made catheter (30.5G needle, 200µm hose), preloaded with heparinized saline (0.5ml heparin [1000 USP units/ml] in 10 ml of sterile saline), was introduced into the tail vein (Fig.11). Scanning was performed for about 45s. About three seconds after the start of the data acquisition, a bolus of 0.1mmol/kg Gd-DTPA in 0.9% NaCl was injected with an infusion pump (AL-1000, WPI, flow rate:2ml/min).

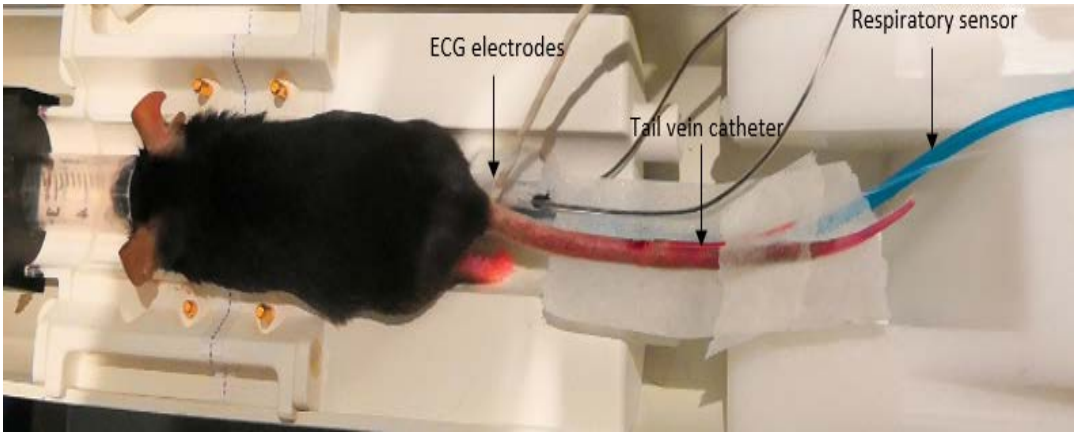

Figure 11: A mouse in the thorax coil. The ECG (electrocardiogram) electrodes, respiratory balloon and the home-made tail vein catheter.

After reconstruction of the first-pass perfusion images, regions of interest (ROI) were placed covering the entire LV lumen and the entire LV ventricle. To avoid partial volume effects, the border regions were excluded from the respective ROI. Signal intensity (SI)-time curves were calculated. The up-slopes $U = (SI_{N\text{-}peak}\text{-}SI_{N\text{-}baseline})/$ heartbeats of the normalized signal intensities $SI_N = (SI\text{-}SI_{min})/(SI_{max}\text{-}SI_{min})$ were calculated.

2.4.4 Reproducibility of Imaging Protocol

For reproducibility assessment of the real-time protocol, rest and dobutamine stress functional imaging were repeated three times on every other day in 3 healthy wild-type mice. LV functional parameters (EDV, ESV, SV, EF, LVMED, LVMES, CO) were quantified from the different temporal resolution protocols (RT1-RT3) and the coefficient of variations (CoV) were quantified.

2.4.5 Data quality analysis

The SNR in the myocardium and the LV blood, the CNR between myocardium and LV blood, and the sharpness over the LV were quantified in all animals for all investigated protocols (IG, RT1-3) in a mid-ventricular slice during end-diastole. To avoid any severe impact of arising streak artifacts and coil sensitivities on the SNR and CNR values, the calculation was performed according to $SNR = \frac{\mu_i}{\sigma_i}$ and $CNR = \frac{\mu_b - \mu_m}{0.5(\sigma_b - \sigma_b)}$, with $\mu_i$and $\sigma_i$being the mean and standard deviation over the LV cavity (μ_b, σ_b) and the myocardium (μ_m, σ_m). Image sharpness was derived from the mean value of a normalized, Sobel filtered fixed ROI encompassing the heart.

2.5 Statistical Analysis

All image analyses were done blinded and data were presented as mean ± standard deviation (SD). Statistical significance of the differences between the reproducibility measurements and the image quality measures (SNR, CNR, image sharpness) were assessed by applying a one-way ANOVA test. The comparison of the functional parameters and the upslope of the myocardial contrast uptake between WT and Het Nexn KO mice were assessed by an unpaired Mann-Whitney U test. Differences were considered statistically significant with p-values < 0.05. For all tests, *$p < 0.05$, **$p < 0.01$, ***$p < 0.001$, ****$p < 0.0001$.

The CoV was calculated as the ratio of standard deviation and the mean value. The reproducibility of the functional parameters was classified according to the CoV value to excellent (CoV < 10%), very good (CoV ≥ 10% and < 15%), good (CoV ≥ 15% and < 20%), moderate (CoV ≥ 20% and < 25%), acceptable (CoV ≥ 25% and < 30%), and poor (CoV ≥ 30%).

3 Results

3.1 Assessment of LV function

The acquisition protocol could be completed in all mice. An example of the resulting image quality for the different imaging protocols is shown for a mid-ventricular slice for one case of Nexn KO Het and WT mice in Fig.12.

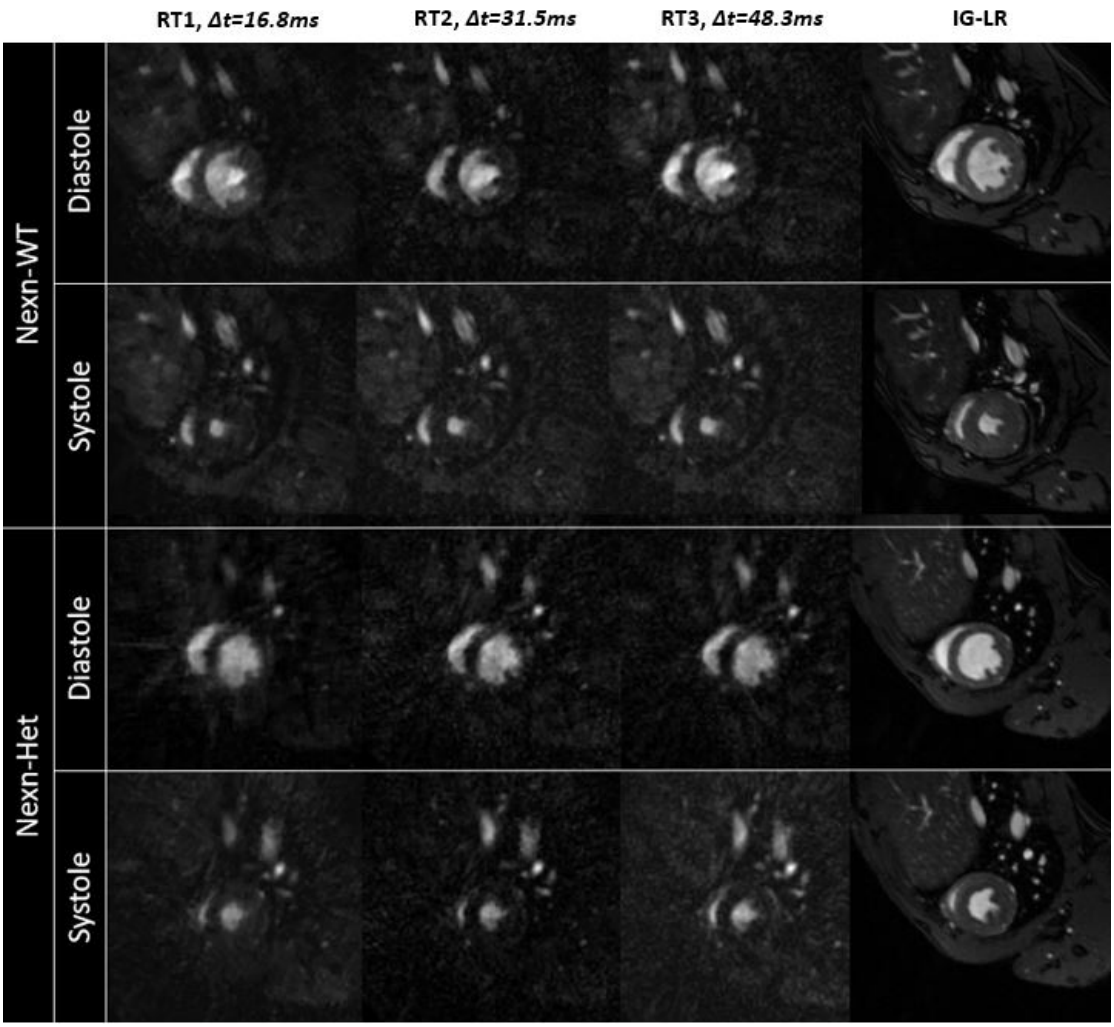

Figure 12: Comparison of the investigated real-time protocols (RT1-3) and the self-gated technique (IG) for mid-slice in one case of Nexn KO Het (heterozygous) and WT (wild-type) mice.

Even though the non-cardiac structures are not clearly visible in the real-time images, the vascular structures as well as the left ventricle can be well appreciated and quantitative assessments of the functional parameters were possible for all investigated real-time protocols. Comparison between the real-time data ($G_3^7 = 8$ (RT1), $G_4^7 = 15$ (RT2), $G_5^7 = 23$ (RT3)) and the self-gating protocols did not reveal any statistically significant differences for all investigated parameters in the Het and WT groups (Fig.13).

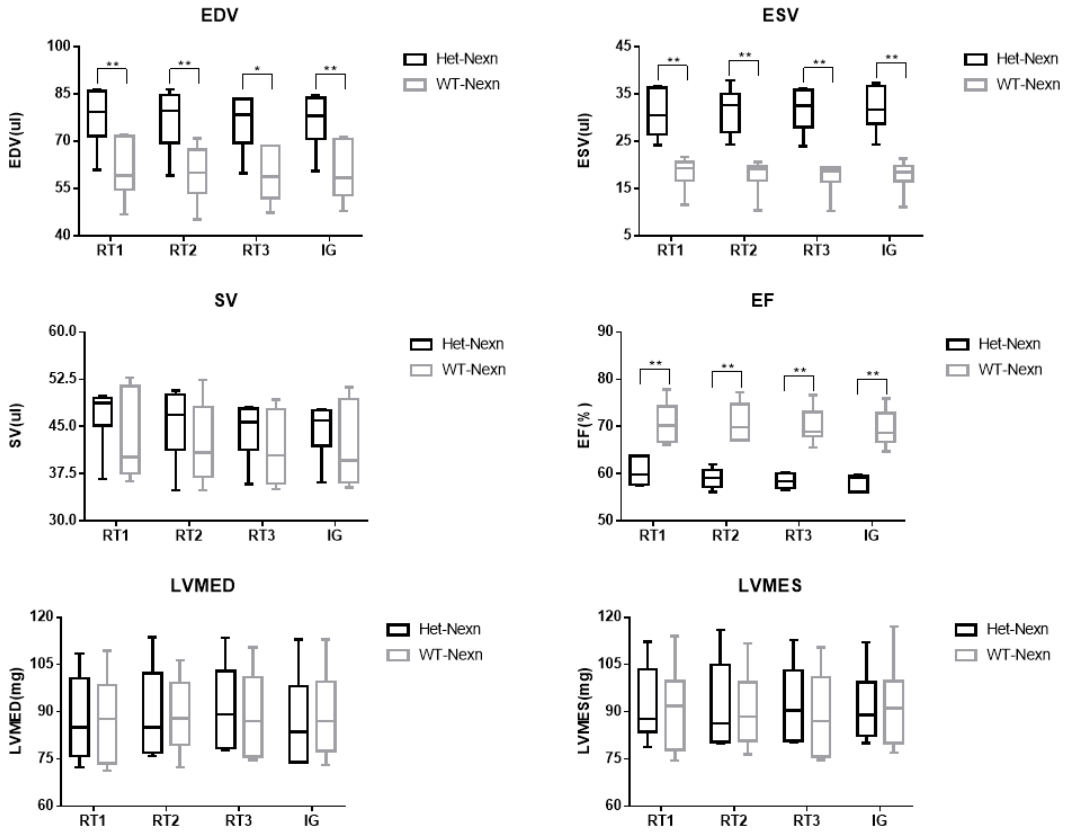

Figure 13: Comparison of cardiac functional parameters (EDV/ESV end-diastolic/systolic volume, SV stroke volume, EF ejection fraction) and left ventricular mass (LVMED/ES end-diastolic/systolic left ventricular mass) for the investigated real-time protocols (RT1-3) and the gated protocols (IG) between Nexn Het (heterozygous) and WT (wild-type) mice.

Compared with WT, the EDV and ESV resulted markedly higher in the Het Nexn-KO mice, resulting in a relatively lower EF ($p < 0.01$). No statistically significant difference for LVM at end-diastole and end-systole were observed between these two groups ($p > 0.05$).

3.2 Dobutamine stress MRI

For the stress investigation, an example of the resulting image quality for the real-time imaging is shown for Nexn Het mice (Fig.14) and Nexn WT mice (Fig.15). A clear decrease of the LV EDV and ESV, and increase of EF but maintained SV after dobutamine injection were observed in both groups (Fig.16).

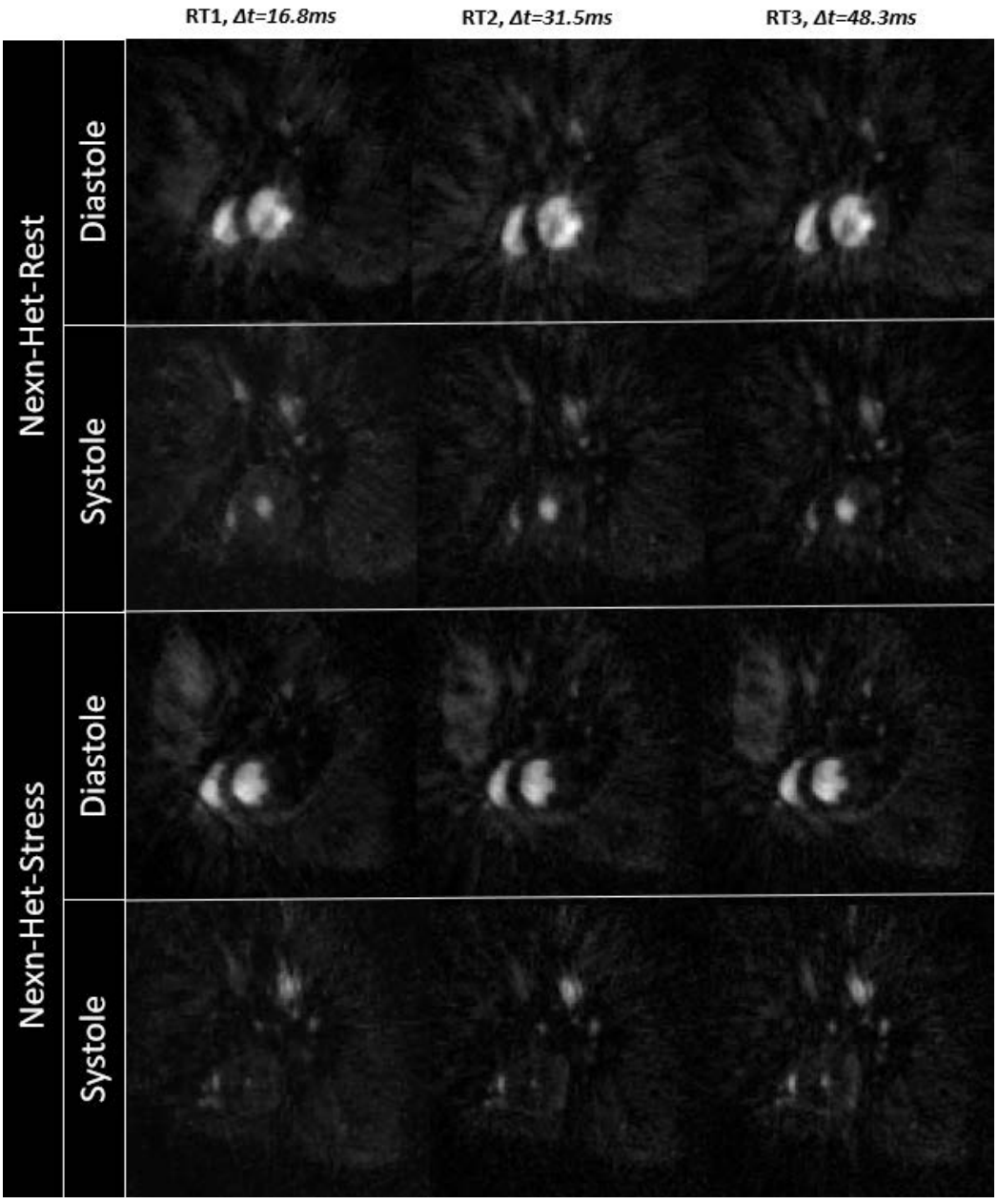

Figure 14: Comparison of the investigated real-time protocols (RT1-3) for mid-slice in one case of Nexn KO Het (heterozygous) mice at baseline and dobutamine stress.

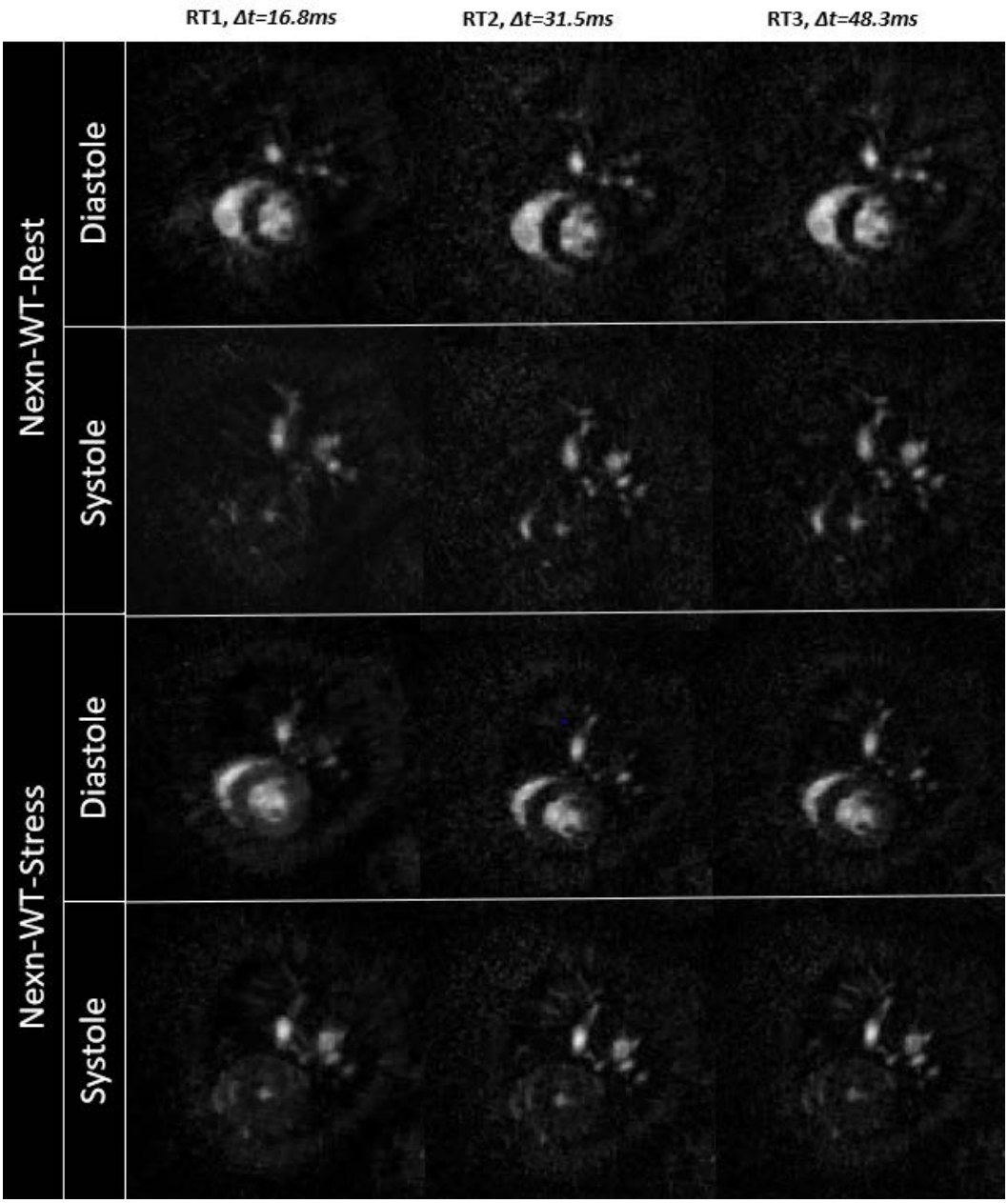

Figure 15: Comparison of the investigated real-time protocols (RT1-3) for mid-slice in one case of Nexn KO WT (wild-type) mice at baseline and dobutamine stress.

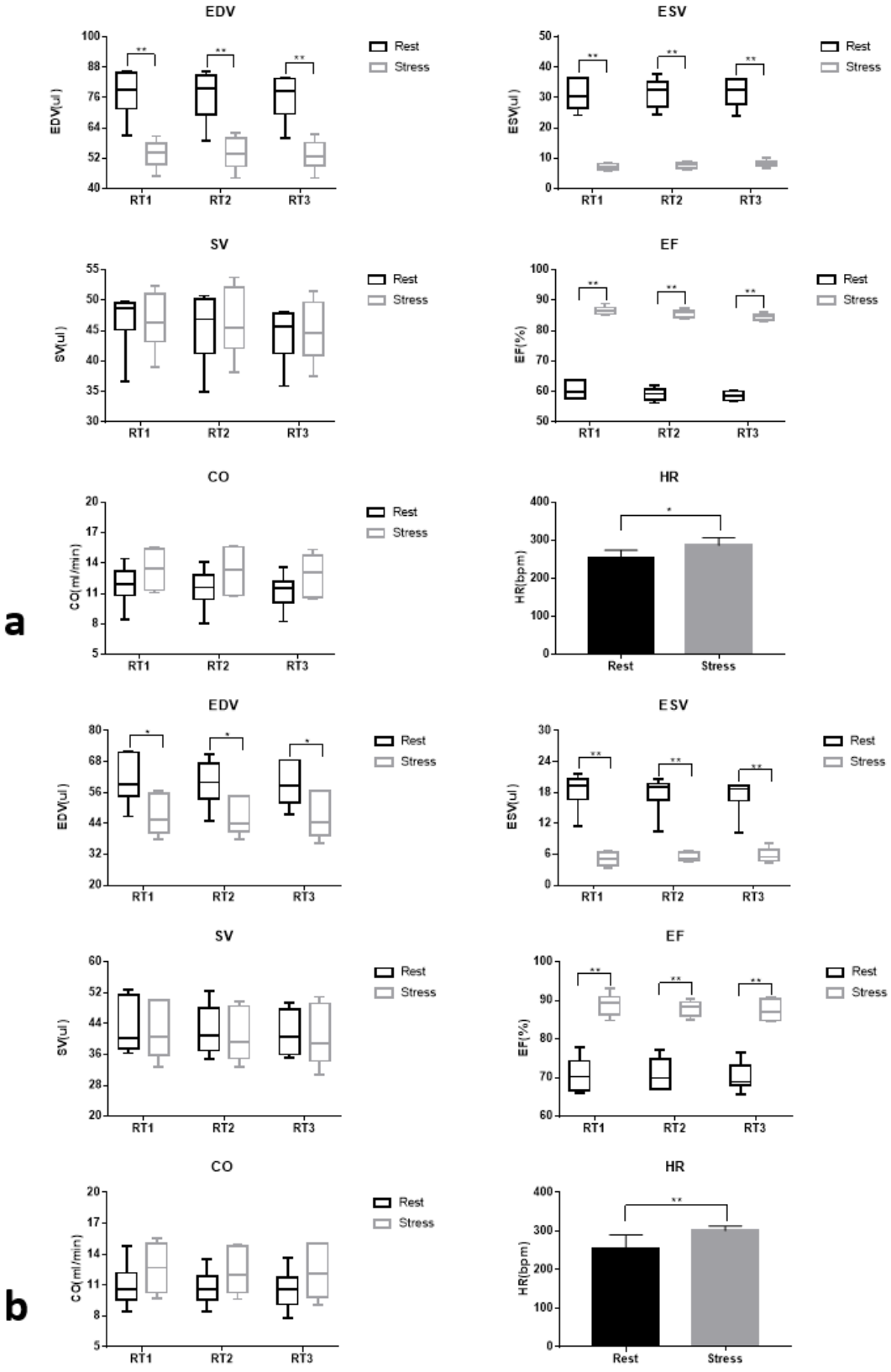

Figure 16: Comparison of cardiac function parameters (EDV/ESV end-diastolic/systolic volume, SV stroke volume, EF ejection fraction, CO cardiac output, HR heart rate) from baseline to dobutamine stress for the investigated real-time protocols (RT1-3) in Nexn mice. **a:** Nexn Het (heterozygous). **b:** Nexn WT (wild type).

Due to the increase of HR (Het, 252.3±22.11 vs. 287.3±20.18; WT, 255.7±34.9 vs. 301.3±11.74), a slightly increase of CO were observed in both groups. Comparison between the different temporal resolution real-time data ($G_3^7 = 8$ (RT1), $G_4^7 = 15$ (RT2), $G_5^7 = 23$ (RT3)) did not reveal any significant differences for all investigated parameters for baseline as well as for dobutamine stress ($p > 0.05$). Compared with Nexn WT, the slightly higher EDV, significantly higher ESV ($p < 0.05$), similar SV and trend to lower EF was observed in Het Nexn-KO mice at stress (Fig.17).

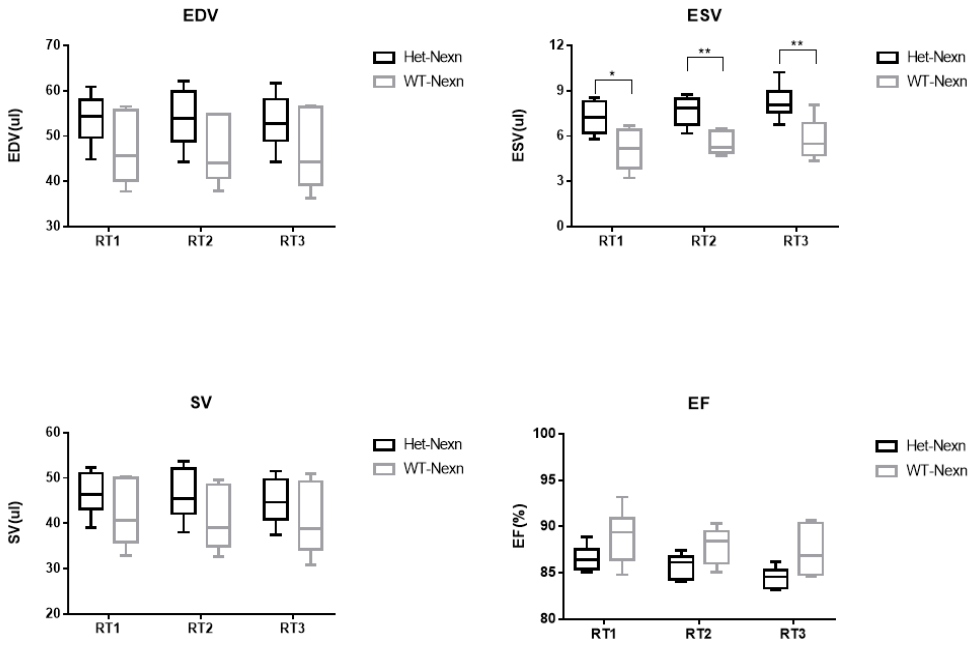

Figure 17: Comparison of cardiac function parameters (EDV/ESV end-diastolic/systolic volume, SV stroke volume, EF ejection fraction) for the investigated real-time protocols (RT1-3) between Nexn Het (heterozygous) and WT (wild-type) mice at dobutamine stress.

3.3 First-pass perfusion MRI

Examples of time-series of myocardial first-pass perfusion images in both groups are provided in Fig.18, illustrating different time points before and after injection of the contrast agent.

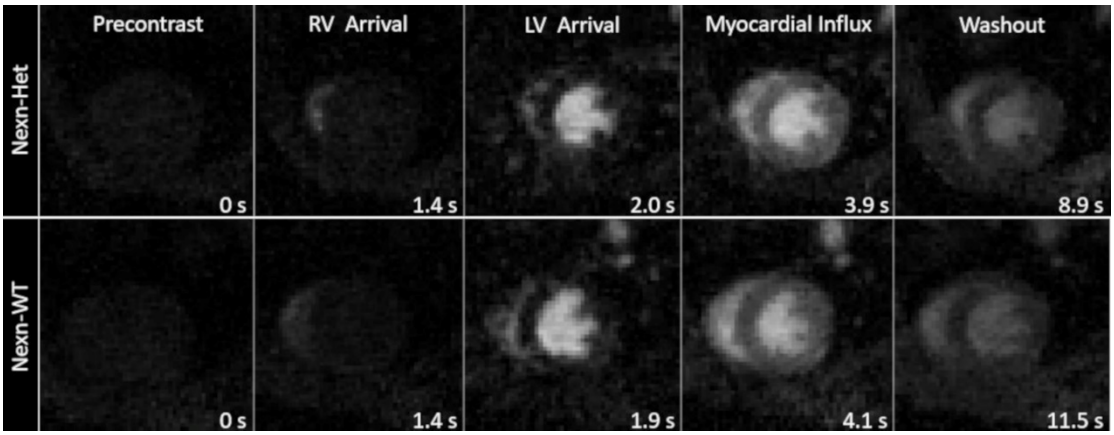

Figure 18: Time series of myocardial first-pass perfusion images of a Nexn Het (heterozygous) and WT (wild-type) mouse. From left to right: precontrast, RV arrival, LV arrival, myocardial influx and washout. (Li et al., 2020b), CC BY-NC 4.0, https://creativecommons.org/licenses/by-nc/4.0/

The blood and myocardial signal are nearly nulled before contrast agent injection by the saturation pulses. The arrival of the contrast agent in RV (1.4s), LV (1.9s), and myocardial influx (4.1s) for Nexn WT and RV (1.4s), LV (2.0s), and myocardial influx (3.9s) for Nexn Het are clearly visible. The signal intensity-time curve of the LV lumen and LV myocardium in Nexn Het and WT mice are shown in Fig.19.

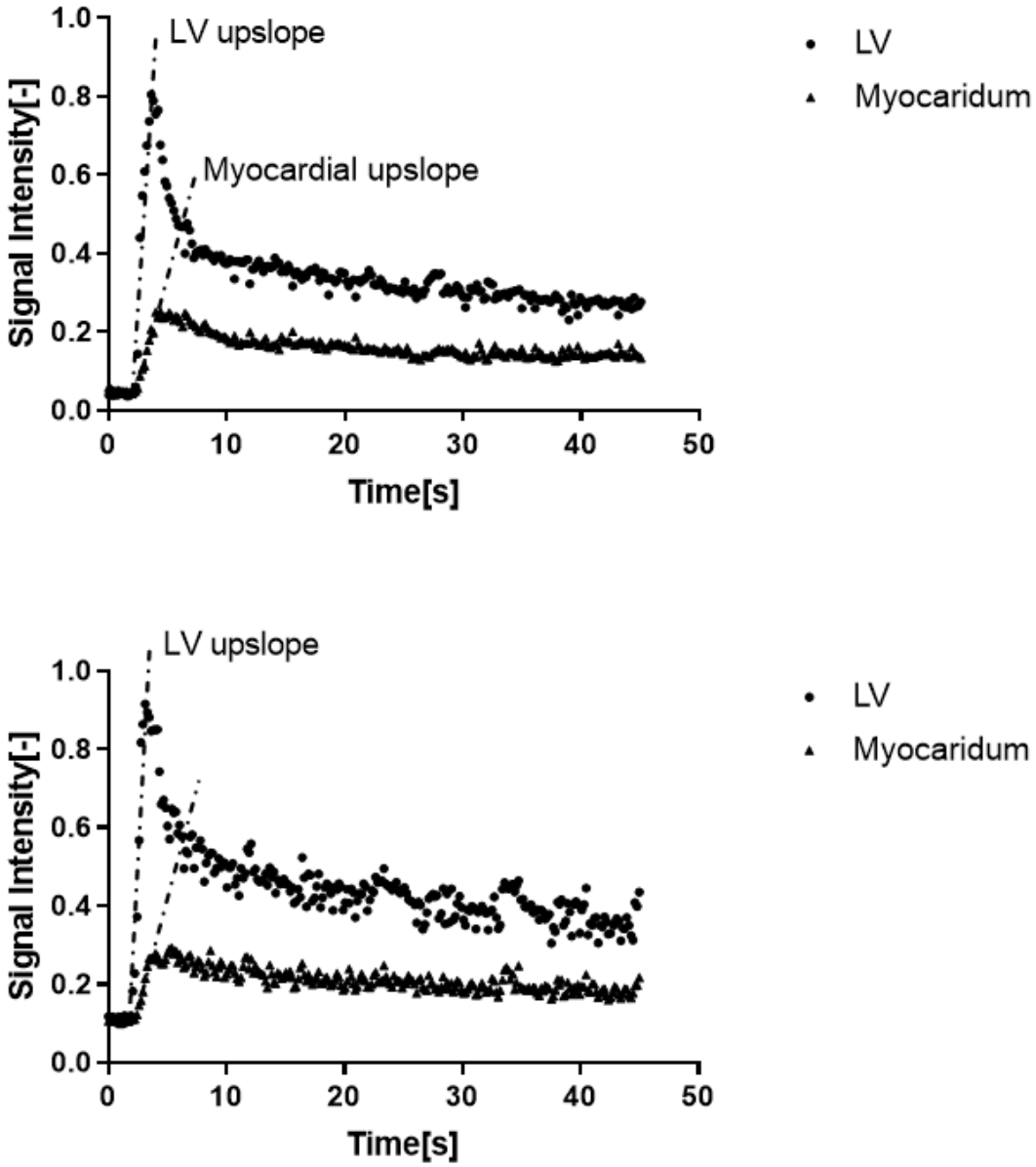

Figure 19: Signal intensity-time curves of LV lumen and LV myocardium exemplarily shown for one Nexn Het (a: heterozygous) and Nexn WT (b: wild-type) mouse. (Li et al., 2020b), CC BY-NC 4.0, https://creativecommons.org/licenses/by-nc/4.0/

The first-pass of contrast agent resulted in a prompt signal increase in the LV lumen. Four to five cardiac cycles later, a gradually signal increase in the LV myocardium could be appreciated, with a peak signal roughly 4s after injection. Analysis of the upslopes in both groups yielded no significantly different (Het, 0.51±0.014; WT, 0.51±0.01; $p > 0.05$) for the LV myocardium (Fig.20).

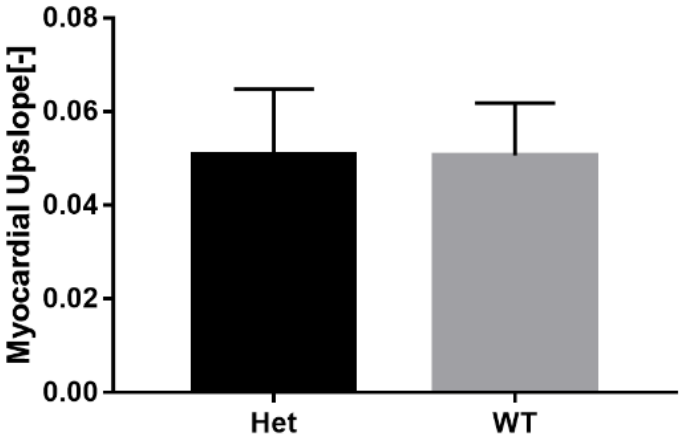

Figure 20: Comparison of normalized signal intensity myocardial upslopes between Nexn KO Het (heterozygous) and WT (wild-type) mice. (Li et al., 2020b), CC BY-NC 4.0, https://creativecommons.org/licenses/by-nc/4.0/

3.4 Reproducibility of Imaging Protocol

No significant difference was observed in all the functional parameters (EDV, ESV, SV, EF, LVMED, LVMES, CO) in RT1-3 protocols at rest (Fig.21) and stress (Fig.22).

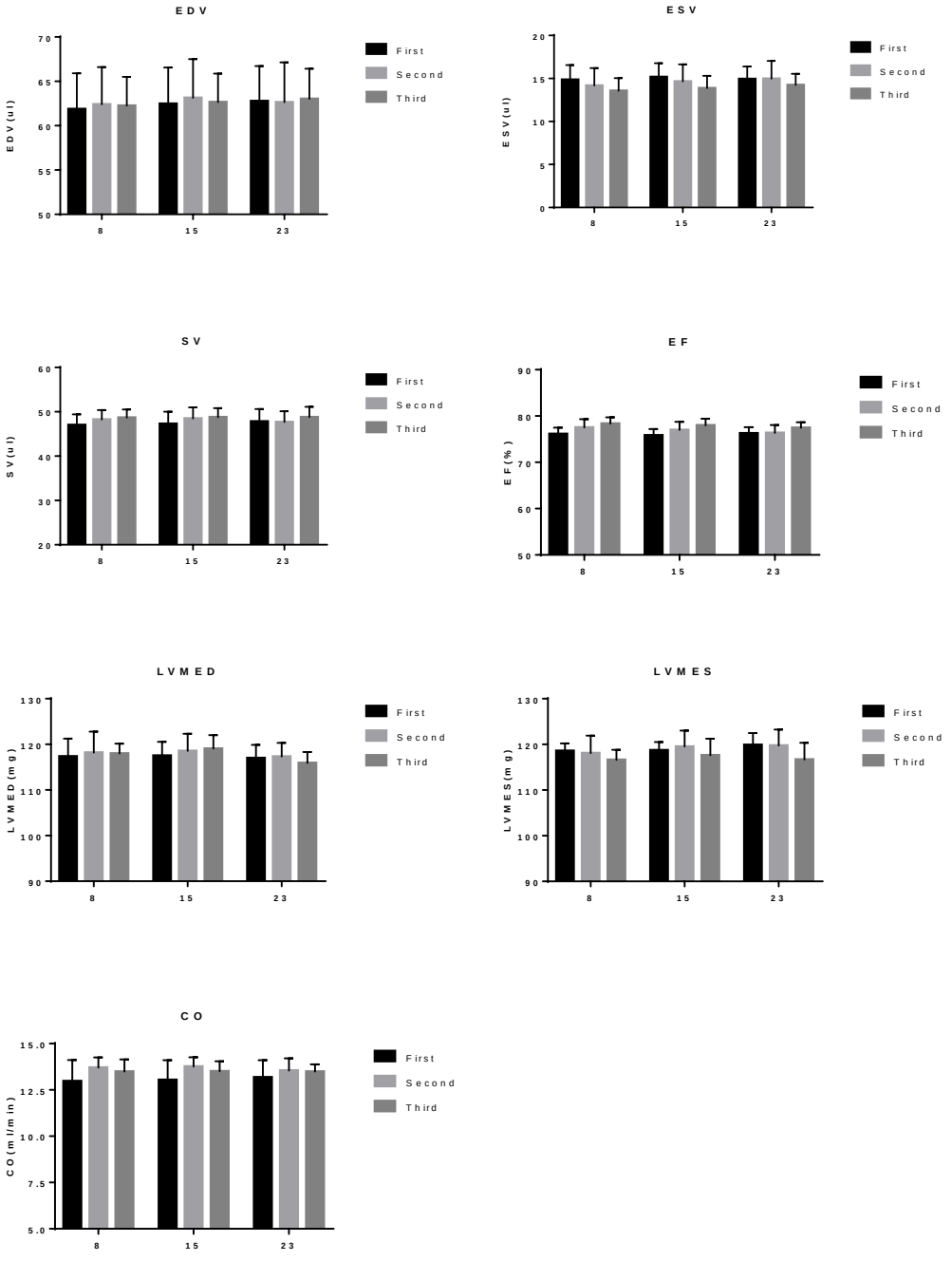

Figure 21: Comparison of cardiac functional parameters (EDV/ESV end-diastolic/systolic volume, SV stroke volume, EF ejection fraction, CO cardiac output) and left ventricular mass (LVMED/ES end-diastolic/systolic left ventricular mass))for the investigated real-time protocols (8: RT1, 15: RT2, 23: RT3) in healthy mice at three consecutive time points at rest.

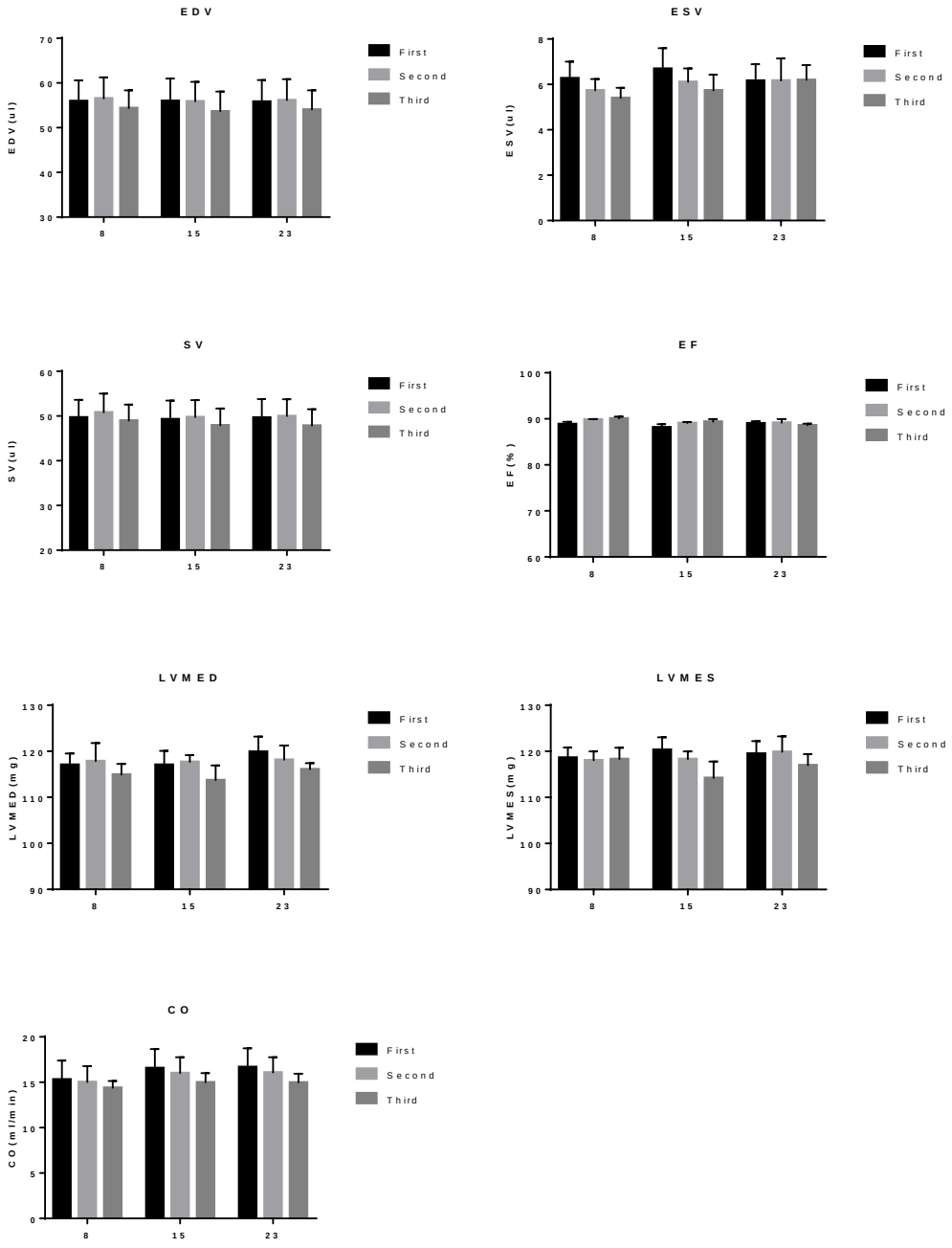

Figure 22: Comparison of cardiac functional parameters (EDV/ESV end-diastolic/systolic volume, SV stroke volume, EF ejection fraction, CO cardiac output) and left ventricular mass (LVMED/ES end-diastolic/systolic left ventricular mass))for the investigated real-time protocols (8: RT1, 15: RT2, 23: RT3) in healthy mice at three consecutive time points at stress.

The identical trends for the functional parameters from baseline to stress are shown in Fig.23.

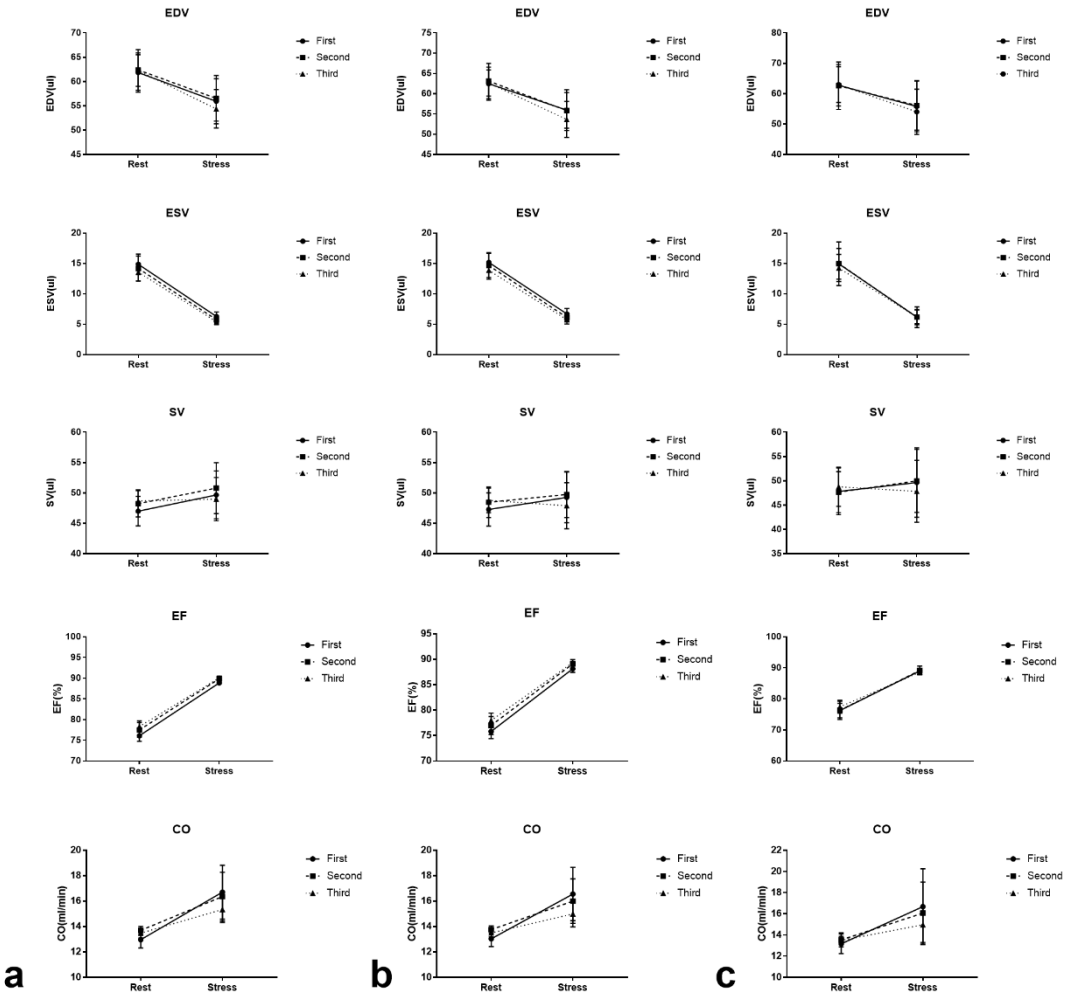

Figure 23: Trend of the functional parameters (EDV/ESV end-diastolic/systolic volume, SV stroke volume, EF ejection fraction, CO cardiac output) from baseline to stress. **a**: $G_3^7 = 8, \Delta t = 16.8ms$. **b**: $G_4^7 = 15, \Delta t = 31.5ms$. **c**: $G_5^7 = 23, \Delta t = 48.3ms$.

One example case from apical to basal slice at rest and stress with different temporal resolution is shown in Figure 24.

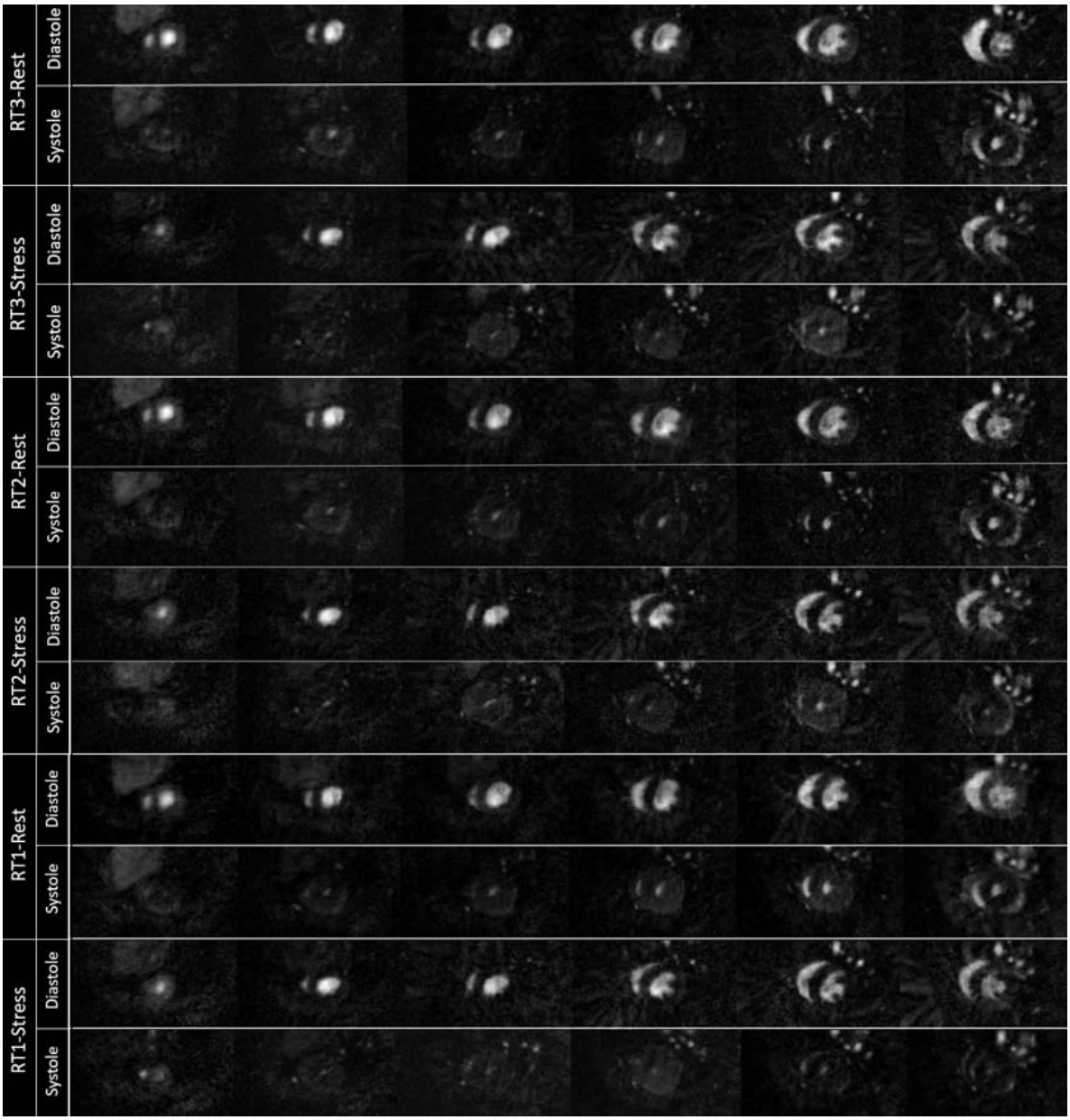

Figure 24: The investigated real-time protocols (RT1-3) from apical to basal slice (from left to right side) of a healthy mouse at rest and stress. RT1: $G_3^7 = 8$, $\Delta t = 16.8ms$; RT2: $G_4^7 = 15$, $\Delta t = 31.5ms$; RT3: $G_5^7 = 23$, $\Delta t = 48.3ms$.

CoV values over all time points for RT1-RT3 at baseline and stress are shown in Table 2 and 3. Please refer to supplementary material for detailed data of all mice. The reproducibility in general was excellent for all functional parameters (EDV, ESV, SV, EF, LVMED, LVMES, CO) in RT1-3 protocols at rest and stress. In one case at stress a slightly reduced (very good) reproducibility for ESV and CO was achieved (supplementary material).

Table 2: CoV(%) of LV function parameters for each investigated real-time protocol over the 3 time points at baseline. RT1: $G_3^7 = 8, \Delta t = 16.8ms$; RT2: $G_4^7 = 15, \Delta t = 31.5ms$; RT3: $G_5^7 = 23, \Delta t = 48.3ms$.

	CoV(EDV)	CoV(ESV)	CoV (SV)	CoV (EF)	CoV(LVMED)	CoV(LVMES)	CoV(CO)
RT1	1.54±0.25	5.30±2.1	1.97±1.5	1.60±0.12	1.77±0.45	1.60±0.57	3.52±3.06
RT2	1.74±0.41	5.28±2.70	1.93±1.33	1.54±0.21	0.87±0.50	1.44±1.06	3.55±3.10
RT3	2.04±1.02	4.38±2.67	2.49±0.71	1.22±0.72	0.73±0.42	1.74±1.05	2.46±2.04

Table 3: CoV(%) of LV function parameters for each investigated real-time protocol over the 3 time points at stress. RT1: $G_3^7 = 8, \Delta t = 16.8ms$; RT2: $G_4^7 = 15, \Delta t = 31.5ms$; RT3: $G_5^7 = 23, \Delta t = 48.3ms$.

	CoV(EDV)	CoV(ESV)	CoV (SV)	CoV (EF)	CoV(LVMED)	CoV(LVMES)	CoV(CO)
RT1	2.01±1.22	7.87±3.47	1.84±1.63	0.85±0.36	1.67±1.07	1.18±0.60	6.13±3.50
RT2	2.7±0.37	8.14±1.54	2.36±0.82	0.82±0.20	2.33±1.56	2.81±1.60	5.80±4.49
RT3	2.13±0.53	4.79±2.76	2.62±0.22	0.71±0.33	1.82±1.22	1.35±0.71	5.75±5.10

3.5 Data quality analysis

No significant differences in SNR, CNR and image sharpness were observed for the investigated real-time protocols RT1-3 (Fig.25). In comparison to the gated approach, the SNR values resulted significantly reduced by about 50%, and a significant but only moderate reduction of the CNR of about 30% was observed for RT1-3. No differences in image sharpness were observed between RT1-3, but a clear reduction by about 50% for end-diastole and a bit more pronounced for the end-systolic case resulted in direct comparison to the gated approach.

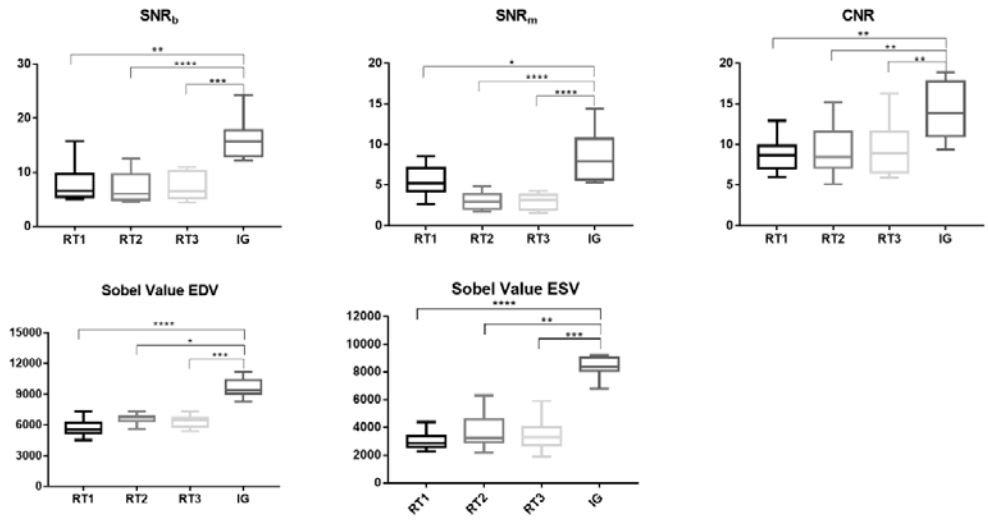

Figure 25: Quantitative image comparison. No significant differences in SNR, CNR and sharpness were observed for the investigated real-time protocols RT1-3. In comparison to the gated approach, the SNR, CNR and Sobel values are significantly reduced in real-time technique. SNR_b: SNR of LV blood pool. SNR_m: SNR of myocardium.

4 Discussion

Even though an established imaging method, small animal cardiac MRI is still a time-consuming technique. Due to the high heart and respiratory rates, the resulting long acquisition time of gated or self-gated techniques limit its application in animal research. The aim of this study is to investigate real time functional cardiac imaging in the mouse model by applying tyGRASP to highly undersampled radial data. The suggested approach could be applied successfully to the quantification of global cardiac function parameters in rest and pharmacological stress as well as first-pass myocardial perfusion imaging.

4.1 TyGRASP in cardiac real-time imaging

After its introduction by Wundrak et al.(Wundrak et al., 2016) in 2016, tyGRASP has been applied in few studies. Haris et al.(Haris et al., 2017) investigated fetal cardiac data of five volunteers at 1.5T by using tyGRASP combined with self-gated cardiac cine MRI. Further, they developed a free-breathing method for retrospective fetal cine MRI using Dopper ultrasound cardiac gating and tyGRASP for accelerated acquisition capable of detecting fetal movements for motion compensation(Haris et al., 2019). Haji-Valiyadeh et al.(Haji-Valizadeh et al., 2018) validate an optimal 12-fold accelerated real-time cine MRI pulse sequence using tyGRASP to produce accurate LV functional parameters in patients at 1.5T and 3T. Jan et al.(Paul et al., 2016) test tyGRASP combine with compressed sensing in real-time imaging to evaluate cardiac function. These experiments certified the feasibility of tyGRASP in cardiac real-time imaging in the clinical application. Due to the property of radial trajectory and real-time imaging, it could enable free-breathing acquisitions and imaging, such as in highly arrhythmic patients or fetal cardiovascular MRI.

For preclinical research, Wech et al.(Wech et al., 2016) investigated the application of radial generalized autocalibrating partially parallel acquisitions (GRAPPA) with large golden angle (111.25°) in real-time imaging. However, in their experiment, only one mid-ventricular slice was investigated in mouse model. For the accurate analysis of cardiac function, the full ventricular coverage is needed. In our study, we firstly applied the tyGRASP in real-time imaging in the Nexn induced heart failure mouse model, and valid its application to accurately evaluate cardiac function.

4.2 Assessment of cardiac function

Mutations in Nexn are associated with cardiomyopathy, especially for the DCM, and resulting in dilated ventricular chambers and impaired contraction(Aherrahrou et al., 2016; Liu et al., 2019). Myocardial damage will finally lead to refractory heart failure and fatal arrhythmia(Weintraub et al., 2017). Because the Nexn deficiency (Homozygous) leads to early postnatal lethality(Aherrahrou et al., 2016), so we only applied our approach in Nexn heterozygous and wild-type mice. Continuous anesthesia during scan is unavoidable for in vivo MRI in the mouse. Many anesthetics may cause respiratory depression and negative chronotropic and inotropic effects(Gargiulo et al., 2012; Massey and Richerson, 2017). In this study, inhalative isoflurane was chosen, which is easy to control and relative sparing effect on cardiovascular function, negligible metabolism, and its faster for induction and recovery(Ludders, 1992).

In our study, a significantly increased EDV (Het, 76.47±8.85; WT, 60.16±9.24; $p < 0.01$, IG), ESV (Het, 31.93±4.71; WT, 17.82±3.48; $p < 0.01$, IG), and decreased EF (Het, 58.36±1.73; WT, 69.5±3.91; $p < 0.01$, IG) could be observed in the Nexn heterozygous mice. But no significantly difference for SV (Het, 44.54±4.38; WT, 41.77±6.67; $p > 0.05$, IG) , end-diastolic left ventricular mass (Het, 86.83±14.69; WT, 89±14.32; $p > 0.05$, IG), end-systolic left ventricular mass (Het, 91.33±11.41; WT, 91.83±14.03; $p > 0.05$, IG) were found between two groups. Comparison between IG and real-time technique (RT1-3), there were no significantly difference among all the investigated cardiac functional parameters.

It could be proven that tyGRASP real-time cardiac MRI in mouse appears feasible for quantification of global functional parameters and enables flexible number of projections for image reconstruction with maximal temporal resolution of 16.8ms ($G_3^7 = 8$) thereby preserving sufficient image quality for quantification of the global function parameters. Similar values without significant differences were obtained by the real-time protocols with reduced temporal resolution.

4.3 Dobutamine stress MRI

Cardiac stress MRI has been applied in preclinical research to detect cardiovascular abnormalities at an early stage(Castle et al., 2019; Guido et al., 2014; Vandsburger et al., 2007; Wiesmann et al., 2001). As real-time imaging offers the rapid and continuous

acquisition of image datasets, it might show advantages for the examination of the immediate response to physiological stress.

The application of the tyGRASP technique in dobutamine stress examinations was tested in Nexn mice, enabling a complete stress examination within a few seconds. Under the effect of β -adrenergic stimulation, there was a significant decrease of both EDV (Het: 30.9% [-]; WT: 22.9% [-]; RT1) and ESV (Het: 76.6% [-]; WT: 72.1% [-]; RT1), also an obviously increase of EF (Het: 43.3% [+]; WT: 25.8% [+]; RT1) in both groups. However, we could not detect apparent changes in stroke volume during dobutamine action, in contrast to human physiology, in which stroke volume can be augmented during β-adrenergic stimulation. Even though we did not have a clear explanation for that, the results are in line with other published mouse experiments(Tyrankiewicz et al., 2013; Wiesmann et al., 2001). Due to the increase of heart rate, a slightly increase of cardiac output could be observed (Het: 12.8% [+]; WT: 15.4% [+]; RT1). Comparison among RT1-3, all the investigated parameters did show significantly difference.

Comparison between Nexn WT and Het mice at dobutamine stress, a relatively higher EDV (Het, 53.14 ± 6.02; WT, 46.38 ± 8.53, $p > 0.05$, RT1), and slightly lower EF (Het, 86.58 ± 1.38; WT, 88.97 ± 2.88, $p > 0.05$, RT1) could be found in Nexn heterozygous group, but without statistically significant. However, the Nexn heterozygous mice still kept a significantly higher ESV (Het, 7.22 ± 1.11; WT, 5.13 ± 1.32, $p < 0.05$, RT1).

The successfully application of our technique in dobutamine stress imaging demonstrates the potential of tyGRASP for real-time cardiac imaging to visualize acute changes of cardiac geometry and function during pharmacologic stimulation.

4.4 First-pass perfusion MRI

Myocardial perfusion MRI is a valuable and safe examination to evaluate the viability of myocardium in patients with suspected or diagnosed ischemic heart disease(Bethke et al., 2019; Sun et al., 2018; Wolff et al., 2004). In preclinical research, especially the mouse model with high heart rate and fast circulation time requires perfusion imaging protocols with high temporal resolution and adequate spatial resolution for the assessment of regional myocardial influx. Coolen et al.(Coolen et al., 2010) and Nierop et al.(van Nierop et al., 2013) estimated the quantitative regional myocardial perfusion values with ECG-triggered, segmented saturation-recovery FISP sequence. They

reported a temporal resolution of 3 cardiac cycles (300-400ms), which might still be insufficient considering the rapid propagation of the bolus within few heartbeats. With the suggested protocol, a temporal resolution of one image per cardiac cycle is achieved, thus improving the temporal fidelity of the inflow and washout quantification. Due to the high heart rate and the fast passage of the contrast agent through the myocardium, we choose the saturation pulses instead of inversion recovery pulses to null the signal. The application of saturation pulses proved effective to generate high contrast between contrast-enhanced and nonenhanced blood and myocardium.

In our study, the normalized upslopes clearly reveal the characteristic difference between blood and myocardium. The first passage of the contrast agent through the right ventricle, left ventricle and myocardium could be observed. In this way, beat-to-beat changes could be achieved. The application of normalized signal intensity removed the influence of small intraexperiment differences in injection speed and dilution of the contrast agent bolus. As the Nexn induced DCM is a non-ischaemic heart disease, as expected we did not find decreased perfusion region of myocardium in first-pass perfusion imaging.

4.5 Assessment of reproducibility

In cardiovascular imaging, variations between different acquisitions remain an important issue when evaluating in vivo data. Especially for longitudinal studies, it is of utmost importance to ensure high reproducibility of the applied method to test a new hypothesis.

Up to now, high-frequency echocardiography remained the most widely used technique to characterize cardiac phenotype of rodents(Moran et al., 2013). However, only limited reports are available on its reproducibility(Collins et al., 2001; Ram et al., 2011; Yang et al., 1999). Factors such as usage of models for final calculation of volumetric data from few two-dimensional slices limit its application in animal models of cardiovascular diseases, especially with abnormal ventricular geometry or heterogeneous regional myocardial function(Amundsen et al., 2011; Ghanem et al., 2006). The full volume acquisition of CMR imaging yield improved reproducibility when compared with geometrical assumptions of echocardiography(Stuckey et al., 2008; van de Weijer et al., 2012).

In our study, the reproducibility measurements revealed excellent reproducibility for all functional parameters. The slightly lower reproducibility (very good) for ESV and CO under stress in one mouse might be attributed to some therapeutic effect of the repeated dobutamine application. The excellent reproducibility reveals that our new approach could be a useful tool for monitoring cardiac diseases in mouse model.

4.6 Assessment of imaging quality

With the acquisition protocol, 192 projections are required for fulfilling Nyquist's theorem. The RT1-3 schemes result to 24 (RT1), 12.8 (RT2), and 8.4 folds undersampling. Even though due to the large flip-angle, the object represented as somehow sparse, the data is still strongly undersampled for all real-time protocols. And even theoretically four-elements are not sufficient for compensating rising artifacts. For compensation of the rising artifacts and improvement of SNR, we applied a CS reconstruction with TV filter along spatial and temporal domain(Wundrak et al., 2016). In pre-experiments we investigated appropriate regularization weighting along both domains, which ensured a) sufficient reduction of streaking artifacts, b) sufficient image quality (SNR, CNR) for subsequent extraction of functional parameters, and c) acceptable levels of regularization artifacts. The parameters were chosen such that all images could be reconstructed without further adaptation of the regularization weighting, thus enabling the application of the technique to cohort studies.

However, the presented approach still resulted in clearly reduced image quality when compared to the conventional self-gated techniques. Even though surrounding structures are not well depicted in the images and remaining streak artifacts are not completely eliminated by the compressed sensing reconstruction, the relevant cardiac structures can be clearly followed over time, and beat to beat changes of functional parameters appear addressable.

Compared with self-gating technique, resulting image quality for the real-time imaging was sufficient for the assessment of functional parameters without significant differences. Even though the image quality is clearly degraded for the real-time approaches, showing reduced SNR and CNR values, it is still sufficient for quantitative analysis of the functional parameters. The spatial resolution of the self-gated protocol is $0.123^2\mathrm{mm}^2$, which is around 40% higher than real-time approach ($\Delta r = 0.2^2\mathrm{mm}^2$). During end-diastole, the reduction of image sharpness complies well with the resolution

compromises done for RT1-3. The slightly increased loss in image sharpness during end-systole can likely be attributed to the rapid contraction of the myocardium causing residual motion even during the short readout time.

4.7 Limitations

There are some limitations to this study. Firstly, during the perfusion acquisition, the tiny fluctuation of the heart rate may result in slightly change of the imaged cardiac phase and some remaining beat to beat differences of the cardiac phase can be appreciated. Secondly, the approach was only tested on a Nexn induced heart failure mouse model and the sensitivity to evaluate changes in perfusion in mouse models with myocardial infarction needs further work.

4.8 Conclusion

In comparison with established standard methods, the highly accelerated real-time CMR imaging with tyGRASP has several advantageous. First, it can significantly reduce the scan time, thus relaxing the load of circulatory challenged animal. Second, the intrinsic low motion artifact level of radial trajectories is of intrinsic advantage for real-time imaging. Third, with the almost incoherent artifacts of the GA approach, in combination with CS reconstruction the number of spokes may be reduced without noticeable effect on the derived parameters. Moreover, the tyGRASP enables data acquisition with optimal k-space coverage and incoherent undersampling artifacts in higher field strength and provides even larger flexibility in the selection of the number of projections to trade temporal resolution vs. image quality for functional imaging as well as perfusion.

In conclusion, real-time cardiac tyGRASP in mice appears feasible with sufficient image quality for quantification of functional parameters. The tyGRASP approach enables flexible number of projections for image reconstruction thus offering the possibility for cardiac rate and phase dependent adjustment of the temporal resolution, which might further optimize the resulting image quality. This protocol can be applied to pharmacological stress or perfusion imaging. It has the potential to reveal real-time and inter-beat variations of the cardiac contraction.

5 Summary

Background: Cardiovascular magnetic resonance (CMR) imaging has proven valuable for the assessment of structural and functional cardiac abnormalities. Even though an established imaging method in small animals, the long acquisition times of gated or self-gated techniques still limit its widespread application. In this study, the application of tiny golden angle radial sparse MRI (tyGRASP) for real-time cardiac imaging in the mouse model was investigated for the quantification of cardiac functional parameters at rest and pharmacological stress, and first-pass perfusion.

Methods: The technique was tested in 12 constitutive nexilin (Nexn) knock-out (KO) mice, heterozygous (Het, N=6) and wild-type (WT, N=6), and the resulting functional parameters compared with the well-established self-gating approach. Real-time images were reconstructed for different temporal resolutions between 16.8ms, 31.5ms and 48.3ms per image. All the mice were additionally scanned after an intraperitoneal injection of 1.5µg/g body weight dobutamine. One week later, first-pass perfusion imaging during intravenous injection of 0.1mmol/kg GD-DTPA was performed. The image quality was investigated between self-gating and real-time techniques. Further, three healthy mice were measured for the assessment of the reproducibility of real-time cardiac functional and dobutamine stress imaging.

Results: In direct comparison with the high-quality self-gated technique, the real-time approach did not show any significant differences in global function parameters at rest or stress for acquisition times below 50ms. Compared with WT, the end-diastolic volume (EDV) and end-systolic volume (ESV) were markedly higher ($p < 0.01$) and the ejection fraction (EF) was significantly lower in the Het Nexn-KO mice at rest ($p < 0.01$). For the stress investigation, a clear decrease of EDV, ESV, and increase of EF but maintained stroke volume (SV) could be observed in both groups. Combined with ECG-triggering, tyGRASP provided first-pass perfusion data with a temporal resolution of one image per heartbeat, allowing the quantitative assessment of upslope curves in the blood-pool and myocardium. Compare with gated approach, the reduction of signal-to-noise ratio, contrast-to-noise ratio and image sharpness could be observed in real-time technique. Excellent reproducibility was achieved in all the functional parameters (CoV < 10%).

Conclusions: The tyGRASP is a valuable real-time MRI technique for mice, which significantly reduces scan time in preclinical cardiac functional imaging, providing sufficient image quality for deriving accurate functional parameters, and has the potential to investigate real-time and beat to beat changes.

6 References

1. Aherrahrou, Z., Schlossarek, S., Stoelting, S., Klinger, M., Geertz, B., Weinberger, F., Kessler, T., Aherrahrou, R., Moreth, K., Bekeredjian, R., Hrabě de Angelis, M., Just, S., Rottbauer, W., Eschenhagen, T., Schunkert, H., Carrier, L., Erdmann, J. (2016). Knock-out of nexilin in mice leads to dilated cardiomyopath Aherrahrou, Z., Schlossarek, S., Stoelting, S., Klinger, M., Geertz, B., Weinberger, F., Kessler, T., Aherrahrou, R., Moreth, K., Bekeredjian, R., Hrabě de Angelis, M., Just, S., Rottbauer, W., Eschenhagen, T., Schunkert, H., Carrier, L., Erdmann, J. (2016). Knock-out of nexilin in mice leads to dilated cardiomyopathy and endomyocardial fibroelastosis. Basic Res Cardiol *111*, 1–10.

2. Amundsen, B.H., Ericsson, M., Seland, J.G., Pavlin, T., Ellingsen, Ø., and Brekken, C. (2011). A comparison of retrospectively self-gated magnetic resonance imaging and high-frequency echocardiography for characterization of left ventricular function in mice. Lab Anim *45*, 31–37.

3. Bethke, A., Shanmuganathan, L., Andersen, G.Ø., Eritsland, J., Swanson, D., Kløw, N.E., and Hoffmann, P. (2019). Microvascular perfusion in infarcted and remote myocardium after successful primary PCI: angiographic and CMR findings. Eur Radiol *29*, 941–950.

4. Biglands, J.D., Radjenovic, A., and Ridgway, J.P. (2012). Cardiovascular magnetic resonance physics for clinicians: part II. J Cardiovasc Magn Reson *14*, 1–40.

5. Bloch, F. (1946). Nuclear Induction. Phys Rev *70*, 460–474.

6. Bollache, E., Barker, A.J., Dolan, R.S., Carr, J.C., van Ooij, P., Ahmadian, R., Powell, A., Collins, J.D., Geiger, J., and Markl, M. (2018). k-t accelerated aortic 4D flow MRI in under two minutes: Feasibility and impact of resolution, k-space sampling patterns, and respiratory navigator gating on hemodynamic measurements: Aortic 4D Flow MRI in Less Than 2 Minutes. Magn Reson Med *79*, 195–207.

7. Breuer, F.A., Kellman, P., Griswold, M.A., and Jakob, P.M. (2005). Dynamic autocalibrated parallel imaging using temporal GRAPPA (TGRAPPA). Magn Reson Med *53*, 981–985.

8. Brinegar, C., Wu, Y.-J.L., Foley, L.M., Hitchens, T.K., Ye, Q., Ho, C., and Liang, Z.-P. (2008). Real-time cardiac MRI without triggering, gating, or breath holding. Conf Proc IEEE Eng Med Biol Soc 2008, 3381–4.

9. Camacho, P., Fan, H., Liu, Z., and He, J.-Q. (2016). Small mammalian animal models of heart disease. Am J Cardiovasc Dis 6, 70–80.

10. Candes, E.J., Romberg, J., and Tao, T. (2006). Robust uncertainty principles: exact signal reconstruction from highly incomplete frequency information. IEEE Trans Inform Theory *52*, 489–509.

11. Castle, P.E., Scheven, U.M., Crouch, A.C., Cao, A.A., Goergen, C.J., and Greve, J.M. (2019). Anatomical location, sex, and age influence murine arterial circumferential cyclic strain before and during dobutamine infusion: Dobutamine Increases Arterial Strain. J Magn Reson Imaging *49*, 69–80.

12. Charoenpanichkit, C., and Hundley, W.G. (2010). The 20 year evolution of dobutamine stress cardiovascular magnetic resonance. J Cardiovasc Magn Reson *12*, 1–16.

13. Chavhan, G.B., Babyn, P.S., Jankharia, B.G., Cheng, H.-L.M., and Shroff, M.M. (2008). Steady-State MR Imaging Sequences: Physics, Classification, and Clinical Applications. RadioGraphics *28*, 1147–1160.

14. Collins, K.A., Korcarz, C.E., Shroff, S.G., Bednarz, J.E., Fentzke, R.C., Lin, H., Leiden, J.M., and Lang, R.M. (2001). Accuracy of echocardiographic estimates of left ventricular mass in mice. Am J Physiol Heart Circ Physiol *280*, H1954–H1962.

15. Coolen, B.F., Moonen, R.P.M., Paulis, L.E.M., Geelen, T., Nicolay, K., and Strijkers, G.J. (2010). Mouse myocardial first-pass perfusion MR imaging. Magn Reson Med *64*, 1658–1663.

16. Currie, S., Hoggard, N., Craven, I.J., Hadjivassiliou, M., and Wilkinson, I.D. (2013). Understanding MRI: basic MR physics for physicians. Postgrad Med J *89*, 209–223.

17. Donoho, D.L. (2006). Compressed sensing. IEEE Trans Inform Theory *52*, 1289–1306.

18. Feng, L., Srichai, M.B., Lim, R.P., Harrison, A., King, W., Adluru, G., Dibella, E.V.R., Sodickson, D.K., Otazo, R., and Kim, D. (2013). Highly accelerated real-time cardiac cine MRI using *k* - *t* SPARSE-SENSE. Magn Reson Med *70*, 64–74.

19. Feng, L., Benkert, T., Block, K.T., Sodickson, D.K., Otazo, R., and Chandarana, H. (2017). Compressed sensing for body MRI: Compressed Sensing for Body MRI. J Magn Reson Imaging *45*, 966–987.

20. Finn, J.P., Nael, K., Deshpande, V., Ratib, O., and Laub, G. (2006). Cardiac MR Imaging: State of the Technology. Radiology *241*, 338–354.

21. Frahm, J., Haase, A., and Matthaei, D. (1986). Rapid NMR imaging of dynamic processes using the FLASII technique. Magn Reson Med *3*, 321–327.

22. Frahm, J., Voit, D., and Uecker, M. (2019). Real-Time Magnetic Resonance Imaging: Radial Gradient-Echo Sequences With Nonlinear Inverse Reconstruction. Invest Radiol 1, 1–10.

23. Frank, D., and Frey, N. (2011). Cardiac Z-disc Signaling Network. J Biol Chem *286*, 9897–9904.

24. Fries, P., Mamann, A., Seidel, R., Müller, A., Stroeder, J., Custodis, F., Reil, J., Schneider, G., and Buecker, A. (2012). Comparison of Retrospectively Self-Gated and Prospectively Triggered FLASH Sequences for Cine Imaging of the Aorta in Mice at 9.4 Tesla. Invest Radiol *47*, 259–266.

25. Gallagher, T.A., Nemeth, A.J., and Hacein-Bey, L. (2008). An Introduction to the Fourier Transform: Relationship to MRI. AJR Am J Roentgenol *190*, 1396–1405.

26. Gargiulo, S., Greco, A., Gramanzini, M., Esposito, S., Affuso, A., Brunetti, A., and Vesce, G. (2012). Mice Anesthesia, Analgesia, and Care, Part I: Anesthetic Considerations in Preclinical Research. ILAR Journal *53*, E55–E69.

27. Ghanem, A., Röll, W., Hashemi, T., Dewald, O., Djoufack, P.C., Fink, K.B., Schrickel, J., Lewalter, T., Lüderitz, B., and Tiemann, K. (2006). Echocardiographic Assessment of Left Ventricular Mass in Neonatal and Adult Mice: Accuracy of Different Echocardiographic Methods. Echocardiography *23*, 900–907.

28. Griswold, M.A., Jakob, P.M., Heidemann, R.M., Nittka, M., Jellus, V., Wang, J., Kiefer, B., and Haase, A. (2002). Generalized autocalibrating partially parallel acquisitions (GRAPPA). Magn Reson Med *47*, 1202–1210.

29. Grobner, T. (2006). Gadolinium – a specific trigger for the development of nephrogenic fibrosing dermopathy and nephrogenic systemic fibrosis? Nephrol Dial Transplant *21*, 1104–1108.

30. Guido, B., I, W.N., G, P.S., O, W.A., Adrian, C.T., J, S.S., and Jennifer, M.A. (2014). Right ventricular dysfunction in the R6/2 transgenic mouse model of Huntington's disease is unmasked by dobutamine. J Huntingtons Dis *3*, 25–32.

31. Haase, A., Frahm, J., Matthaei, D., Hänicke, W., and Merboldt, K.-D. (1986). FLASH imaging: Rapid NMR imaging using low flip-angle pulses. J Magn Reson *67*, 258–266.

32. Haji-Valizadeh, H., Rahsepar, A.A., Collins, J.D., Bassett, E., Isakova, T., Block, T., Adluru, G., DiBella, E.V.R., Lee, D.C., Carr, J.C., et al. (2018). Validation of highly accelerated real-time cardiac cine MRI with radial k-space sampling and compressed sensing in patients at 1.5T and 3T: Real-Time Cine MRI Using Radial k-Space Sampling and Compressed Sensing. Magn Reson Med *79*, 2745–2751.

33. Haris, K., Hedström, E., Bidhult, S., Testud, F., Maglaveras, N., Heiberg, E., Hansson, S.R., Arheden, H., and Aletras, A.H. (2017). Self-gated fetal cardiac MRI with tiny golden angle iGRASP: A feasibility study: Self-Gated Fetal Cardiac MRI With iGRASP. J Magn Reson Imaging *46*, 207–217.

34. Haris, K., Hedström, E., Kording, F., Bidhult, S., Steding-Ehrenborg, K., Ruprecht, C., Heiberg, E., Arheden, H., and Aletras, A.H. (2019). Free-breathing fetal cardiac MRI with doppler ultrasound gating, compressed sensing, and motion compensation: Free-Breathing Fetal Cardiac MRI. J Magn Reson Imaging. 6, 1–13.

35. Hassel, D., Dahme, T., Erdmann, J., Meder, B., Huge, A., Stoll, M., Just, S., Hess, A., Ehlermann, P., Weichenhan, D., Grimmler, M., Liptau, H., Hetzer, R., Regitz-Zagrosek, V., Fischer, C., Nürnberg, P., Schunkert, H., Katus, HA., Rottbauer, W. (2009). Nexilin mutations destabilize cardiac Z-disks and lead to dilated cardiomyopathy. Nat Med *15*, 1281–1288.

36. Heiberg, E., Sjögren, J., Ugander, M., Carlsson, M., Engblom, H., and Arheden, H. (2010). Design and validation of Segment - freely available software for cardiovascular image analysis. BMC Med Imaging *10*, 1-13.

37. Hernandez, L.E. (2018). Myocardial stress perfusion magnetic resonance in children with hypertrophic cardiomyopathy. Cardiol Young *28*, 702–708.

38. Hiba, B., Richard, N., Janier, M., and Croisille, P. (2006). Cardiac and respiratory double self-gated cine MRI in the mouse at 7 T. Magn Reson Med *55*, 506–513.

39. Joubert, M., Tager, P., Legallois, D., Defourneaux, E., Le Guellec, B., Gerber, B., Morello, R., and Manrique, A. (2017). Test-retest reproducibility of cardiac magnetic resonance imaging in healthy mice at 7-Tesla: effect of anesthetic procedures. Sci Rep *7*, 1-11.

40. Kido, T., Kido, T., Nakamura, M., Watanabe, K., Schmidt, M., Forman, C., and Mochizuki, T. (2016). Compressed sensing real-time cine cardiovascular magnetic resonance: accurate

assessment of left ventricular function in a single-breath-hold. J Cardiovasc Magn Reson *18*, 1-11.

41. Kober, F., Iltis, I., Cozzone, P.J., and Bernard, M. (2005). Myocardial blood flow mapping in mice using high-resolution spin labeling magnetic resonance imaging: Influence of ketamine/xylazine and isoflurane anesthesia. Magn Reson Med *53*, 601–606.

42. Kober, F., Jao, T., Troalen, T., and Nayak, K.S. (2016). Myocardial arterial spin labeling. J Cardiovasc Magn Reson *18*, 1–16.

43. Kwiatkowski, G., and Kozerke, S. (2019). Extended quantitative dynamic contrast-enhanced cardiac perfusion imaging in mice using accelerated data acquisition and spatially distributed, two-compartment exchange modeling. NMR Biomed e4123, 1–14.

44. Le, T.-T., Huang, W., Bryant, J.A., Cook, S.A., and Chin, C.W.-L. (2017). Stress cardiovascular magnetic resonance imaging: current and future perspectives. Expert Rev Cardiovasc Ther *15*, 181–189.

45. Li, H., Abaei, A., Metze, P., Just, S., Lu, Q., and Rasche, V. (2020a). Technical Aspects of in vivo Small Animal CMR Imaging. Front. Phys. *8*, 183.

46. Li, H., Metze, P., Abaei, A., Rottbauer, W., Just, S., Lu, Q., and Rasche, V. (2020b). Feasibility of real-time cardiac MRI in mice using tiny golden angle radial sparse. NMR in Biomedicine e4300.

47. Liu, C., Spinozzi, S., Chen, J.-Y., Fang, X., Feng, W., Perkins, G., Cattaneo, P., Guimarães-Camboa, N., Dalton, N.D., Peterson, K.L., Wu, T., Ouyang, K., Fu, XD., Evans, SM., Chen, J. (2019). Nexilin is a New Component of Junctional Membrane Complexes Required for Cardiac T-Tubule Formation. Circulation *140*, 55–66.

48. Ludders, J.W. (1992). Advantages and Guidelines for Using Isoflurane. Vet Clin North Am Small Anim Pract *22*, 328–331.

49. Lustig, M., Donoho, D., and Pauly, J.M. (2007). Sparse MRI: The application of compressed sensing for rapid MR imaging. Magn Reson Med *58*, 1182–1195.

50. Lustig, M., Donoho, D.L., Santos, J.M., and Pauly, J.M. (2008). Compressed Sensing MRI. IEEE Signal Process Mag *25*, 72–82.

51. Massey, C.A., and Richerson, G.B. (2017). Isoflurane, ketamine-xylazine, and urethane markedly alter breathing even at subtherapeutic doses. J Neurophysiol *118*, 2389–2401.

52. McNally, E.M., and Mestroni, L. (2018). Dilated cardiomyopathy: genetic determinants and mechanisms. Circ Res *121*, 731–748.

53. Messroghli, D.R., Moon, J.C., Ferreira, V.M., Grosse-Wortmann, L., He, T., Kellman, P., Mascherbauer, J., Nezafat, R., Salerno, M., Schelbert, E.B., Taylor, A.J., Thompson, R., Ugander, M., van Heeswijk, R.B., Friedrich, M.G. (2017). Clinical recommendations for cardiovascular magnetic resonance mapping of T1, T2, T2* and extracellular volume: A consensus statement by the Society for Cardiovascular Magnetic Resonance (SCMR) endorsed by the European Association for Cardiovascular Imaging (EACVI). J Cardiovasc Magn Reson *19*, 1–24.

54. van der Meulen, P., Groen, J.P., and Cuppen, J.J.M. (1985). Very fast MR imaging by field echoes and small angle excitation. Magn Reson Imaging *3*, 297–299.

55. Milani-Nejad, N., and Janssen, P.M.L. (2014). Small and large animal models in cardiac contraction research: Advantages and disadvantages. Pharmacol Ther *141*, 235–249.

56. Moran, C.M., Thomson, A.J.W., Rog-Zielinska, E., and Gray, G.A. (2013). High-resolution echocardiography in the assessment of cardiac physiology and disease in preclinical models: High-resolution echocardiography in preclinical models. Exp Physiol *98*, 629–644.

57. Nesser, H.-J., Mor-Avi, V., Gorissen, W., Weinert, L., Steringer-Mascherbauer, R., Niel, J., Sugeng, L., and Lang, R.M. (2009). Quantification of left ventricular volumes using three-dimensional echocardiographic speckle tracking: comparison with MRI. Eur Heart J *30*, 1565–1573.

58. Niemann, P.S., Pinho, L., Balbach, T., Galuschky, C., Blankenhagen, M., Silberbach, M., Broberg, C., Jerosch-Herold, M., and Sahn, D.J. (2007). Anatomically Oriented Right Ventricular Volume Measurements with Dynamic Three-Dimensional Echocardiography Validated by 3-Tesla Magnetic Resonance Imaging. J Am Coll Cardiol *50*, 1668–1676.

59. van Nierop, B.J., Coolen, B.F., Dijk, W.J.R., Hendriks, A.D., de Graaf, L., Nicolay, K., and Strijkers, G.J. (2013). Quantitative first-pass perfusion MRI of the mouse myocardium: Quantitative First-Pass Perfusion MRI. Magn Reson Med *69*, 1735–1744.

60. Otazo, R., Kim, D., Axel, L., and Sodickson, D.K. (2010). Combination of compressed sensing and parallel imaging for highly accelerated first-pass cardiac perfusion MRI. Magn Reson Med *64*, 767–776.

61. Palmer, O.R., Chiu, C.B., Cao, A., Scheven, U.M., Diaz, J.A., and Greve, J.M. (2017). In vivo characterization of the murine venous system before and during dobutamine stimulation: implications for preclinical models of venous disease. Ann Anat *214*, 43–52.

62. Paul, J., Schmitt, V., Wundrak, S., Radermacher, M., Hombach, V., Bernhardt, P., Rottbauer, W., and Rasche, V. (2016). Realtime cardiac function using compressed sensing: initial clinical evaluation. J Cardiovasc Magn Reson *18*, suppl 1, 1–3.

63. Petersen, S.E., Aung, N., Sanghvi, M.M., Zemrak, F., Fung, K., Paiva, J.M., Francis, J.M., Khanji, M.Y., Lukaschuk, E., Lee, A.M., Carapella, V., Kim, Y.J., Leeson, P., Piechnik, S.K., Neubauer, S. (2017). Reference ranges for cardiac structure and function using cardiovascular magnetic resonance (CMR) in Caucasians from the UK Biobank population cohort. J Cardiovasc Magn Reson *19*, 1–19.

64. Peterzan, M.A., Rider, O.J., and Anderson, L.J. (2016). The Role of Cardiovascular Magnetic Resonance Imaging in Heart Failure. Card Fail Rev *2*, 115–122.

65. Plewes, D.B., and Kucharczyk, W. (2012). Physics of MRI: A primer. J Magn Reson Imaging *35*, 1038–1054.

66. Purcell, E.M., Torrey, H.C., and Pound, R.V. (1946). Resonance Absorption by Nuclear Magnetic Moments in a Solid. Phys Rev *69*, 37–38.

67. Ram, R., Mickelsen, D.M., Theodoropoulos, C., and Blaxall, B.C. (2011). New approaches in small animal echocardiography: imaging the sounds of silence. Am J Physiol Heart Circ Physiol *301*, H1765–H1780.

68. Ridgway, J.P. (2010). Cardiovascular magnetic resonance physics for clinicians: part I. J Cardiovasc Magn Reson *12*, 1–28.

69. Rose, S.E., Wilson, S.J., Zelaya, F.O., Crozier, S., and Doddrell, D.M. (1994). High resolution high field rodent cardiac imaging with flow enhancement suppression. Magn Reson Imaging *12*, 1183–1190.

70. Saab, R., and Hage, F.G. (2017). Vasodilator stress agents for myocardial perfusion imaging. J Nucl Cardiol *24*, 434–438.

71. Schneider, J.E., Cassidy, P.J., Lygate, C., Tyler, D.J., Wiesmann, F., Grieve, S.M., Hulbert, K., Clarke, K., and Neubauer, S. (2003). Fast, high-resolution in vivo cine magnetic resonance imaging in normal and failing mouse hearts on a vertical 11.7 T system. J Magn Reson Imaging *18*, 691–701.

72. Schnell, S., Markl, M., Entezari, P., Mahadewia, R.J., Semaan, E., Stankovic, Z., Collins, J., Carr, J., and Jung, B. (2014). *k-t* GRAPPA accelerated four-dimensional flow MRI in the aorta: Effect on scan time, image quality, and quantification of flow and wall shear stress: *k-t* GRAPPA Acceleration and Hemodynamics. Magn Reson Med *72*, 522–533.

73. Schultheiss, H.-P., Fairweather, D., Caforio, A.L.P., Escher, F., Hershberger, R.E., Lipshultz, S.E., Liu, P.P., Matsumori, A., Mazzanti, A., McMurray, J., et al. (2019). Dilated cardiomyopathy. Nat Rev Dis Primers *5*, 1–19.

74. Seiberlich, N., Ehses, P., Duerk, J., Gilkeson, R., and Griswold, M. (2011). Improved radial GRAPPA calibration for real-time free-breathing cardiac imaging. Magn Reson Med *65*, 492–505.

75. Streif, J.U.G., Nahrendorf, M., Hiller, K.-H., Waller, C., Wiesmann, F., Rommel, E., Haase, A., and Bauer, W.R. (2005). In vivo assessment of absolute perfusion and intracapillary blood volume in the murine myocardium by spin labeling magnetic resonance imaging. Magn Reson Med *53*, 584–592.

76. Stuckey, D.J., Carr, C.A., Tyler, D.J., and Clarke, K. (2008). Cine-MRI versus two-dimensional echocardiography to measure *in vivo* left ventricular function in rat heart. NMR Biomed *21*, 765–772.

77. Stuckey, D.J., Carr, C.A., Camelliti, P., Tyler, D.J., Davies, K.E., and Clarke, K. (2012). In vivo MRI Characterization of Progressive Cardiac Dysfunction in the mdx Mouse Model of Muscular Dystrophy. PLoS One *7*, e28569, 1–8.

78. Sugeng, L., Mor-Avi, V., Weinert, L., Niel, J., Ebner, C., Steringer-Mascherbauer, R., Schmidt, F., Galuschky, C., Schummers, G., Lang, R.M., Nesser, H.J. (2006). Quantitative Assessment of Left Ventricular Size and Function: Side-by-Side Comparison of Real-Time Three-Dimensional Echocardiography and Computed Tomography With Magnetic Resonance Reference. Circulation *114*, 654–661.

79. Sun, W., Sun, L., Yang, F., Zhao, X., Cai, R., and Yuan, W. (2018). Evaluation of myocardial viability in myocardial infarction patients by magnetic resonance perfusion and delayed enhancement imaging. Herz *10*, 1-8.

80. Longmore DB, Klipstein RH, Underwood SR, Firmin DN, Hounsfield GN, Watanabe M, Bland C, Fox K, Poole-Wilson PA, Rees RS, Denison D, Mcneilly AM, Burman ED. (1985).Dimensional accuracy of magnetic resonance in studies of the heart. Lancet *15*, 1360-1362.

81. Tyrankiewicz, U., Skorka, T., Jablonska, M., Petkow-Dimitrow, P., and Chlopicki, S. (2013). Characterization of the cardiac response to a low and high dose of dobutamine in the mouse model of dilated cardiomyopathy by MRI in vivo. J Magn Reson Imaging *37*, 669–677.

82. Uecker, M., Zhang, S., Voit, D., Karaus, A., Merboldt, K.-D., and Frahm, J. (2010). Real-time MRI at a resolution of 20 ms. NMR Biomed *23*, 986–994.

83. Uecker, M., Zhang, S., Voit, D., Merboldt, K.-D., and Frahm, J. (2012). Real-time MRI: recent advances using radial FLASH. Imaging Med *4*, 461–476.

84. Vandsburger, M.H., French, B.A., Helm, P.A., Roy, R.J., Kramer, C.M., Young, A.A., and Epstein, F.H. (2007). Multi-parameter in vivo cardiac magnetic resonance imaging demonstrates normal perfusion reserve despite severely attenuated β-adrenergic functional response in neuronal nitric oxide synthase knockout mice. Eur Heart J *28*, 2792–2798.

85. Vanhoutte, L., Gallez, B., Feron, O., Balligand, J.-L., Esfahani, H., d'Hoore, W., and Moniotte, S. (2015). Variability of Mouse Left Ventricular Function Assessment by 11.7 Tesla MRI. J Cardiovasc Transl Res *8*, 362–371.

86. Vincenti, G., Masci, P.G., Monney, P., Rutz, T., Hugelshofer, S., Gaxherri, M., Muller, O., Iglesias, J.F., Eeckhout, E., Lorenzoni, V., Pellaton, C., Sierro, C., Schwitter, J. (2017). Stress Perfusion CMR in Patients With Known and Suspected CAD. JACC Cardiovasc Imaging *10*, 526–537.

87. Wech, T., Seiberlich, N., Schindele, A., Grau, V., Diffley, L., Gyngell, M.L., Borzì, A., Köstler, H., and Schneider, J.E. (2016). Development of Real-Time Magnetic Resonance Imaging of Mouse Hearts at 9.4 Tesla – Simulations and First Application. IEEE Trans Med Imaging *35*, 912–920.

88. van de Weijer, T., van Ewijk, P.A., Zandbergen, H.R., Slenter, J.M., Kessels, A.G., Wildberger, J.E., Hesselink, M.K.C., Schrauwen, P., Schrauwen-Hinderling, V.B., and Kooi, M.E. (2012). Geometrical models for cardiac MRI in rodents: comparison of quantification of left ventricular volumes and function by various geometrical models with a full-volume MRI data set in rodents. Am J Physiol Heart Circ Physiol *302*, H709–H715.

89. Weintraub, R.G., Semsarian, C., and Macdonald, P. (2017). Dilated cardiomyopathy. Lancet *390*, 400–414.

90. Wessels, A., and Sedmera, D. (2003). Developmental anatomy of the heart: a tale of mice and man. Physiol Genomics *15*, 165–176.

91. Wiesmann, F., Ruff, J., Engelhardt, S., Hein, L., Dienesch, C., Leupold, A., Illinger, R., Frydrychowicz, A., Hiller, K.-H., Rommel, E., Haase, A., Lohse, M.J., Neubauer, S. (2001). Dobutamine-Stress Magnetic Resonance Microimaging in Mice: Acute Changes of Cardiac Geometry and Function in Normal and Failing Murine Hearts. Circ Res *88*, 563–569.

92. Winkelmann, S., Schaeffter, T., Koehler, T., Eggers, H., and Doessel, O. (2007). An Optimal Radial Profile Order Based on the Golden Ratio for Time-Resolved MRI. IEEE Trans Med Imaging *26*, 68–76.

93. Wolff, S.D., Schwitter, J., Coulden, R., Friedrich, M.G., Bluemke, D.A., Biederman, R.W., Martin, E.T., Lansky, A.J., Kashanian, F., Foo, T.K., Licato, P.E., Comeau, C.R. (2004). Myocardial First-Pass Perfusion Magnetic Resonance Imaging: A Multicenter Dose-Ranging Study. Circulation *110*, 732–737.

94. Wundrak, S., Paul, J., Ulrici, J., Hell, E., and Rasche, V. (2015). A Small Surrogate for the Golden Angle in Time-Resolved Radial MRI Based on Generalized Fibonacci Sequences. IEEE Trans Med Imaging *34*, 1262–1269.

95. Wundrak, S., Paul, J., Ulrici, J., Hell, E., Geibel, M.-A., Bernhardt, P., Rottbauer, W., and Rasche, V. (2016). Golden ratio sparse MRI using tiny golden angles: Golden Ratio Sparse MRI Using Tiny Golden Angles. Magn Reson Med *75*, 2372–2378.

96. Xue, H., Kellman, P., LaRocca, G., Arai, A.E., and Hansen, M.S. (2013). High spatial and temporal resolution retrospective cine cardiovascular magnetic resonance from shortened free breathing real-time acquisitions. J Cardiovasc Magn Reson *15*, 1–15.

97. Yang, X.-P., Liu, Y.-H., Rhaleb, N.-E., Kurihara, N., Kim, H.E., and Carretero, O.A. (1999). Echocardiographic assessment of cardiac function in conscious and anesthetized mice. Am J Physiol *277*, H1967–H1974.

98. Zhang, S., Uecker, M., Voit, D., Merboldt, K.-D., and Frahm, J. (2010). Real-time cardiovascular magnetic resonance at high temporal resolution: radial FLASH with nonlinear inverse reconstruction. J Cardiovasc Magn Reson *12*, 1–7.

99. Zhang, Y., Hetherington, H.P., Stokely, E.M., Mason, G.F., and Twieg, D.B. (1998). A novelk-space trajectory measurement technique. Magn Reson Med *39*, 999–1004.

100. Zuo, Z., Subgang, A., Abaei, A., Rottbauer, W., Stiller, D., Ma, G., and Rasche, V. (2017). Assessment of Longitudinal Reproducibility of Mice LV Function Parameters at 11.7 T Derived from Self-Gated CINE MRI. Biomed Res Int *2017*, 1–10.

101. Zur, Y., Wood, M.L., and Neuringer, L.J. (1991). Spoiling of transverse magnetization in steady-state sequences. Magn Reson Med *21*, 251–263.

7 Supplementary Material

Table 4: CoV(%) of LV function parameters for each investigated mouse over the 3 time points at baseline with RT1 protocol. RT1: $G37$=8, Δt=16.8ms.

	CoV(EDV)	CoV(ESV)	CoV (SV)	CoV (EF)	CoV(LVMED)	CoV(LVMES)	CoV(CO)
Mouse 1	1.35	6.23	2.31	1.57	1.30	1.73	6.55
Mouse 2	1.46	6.77	0.33	1.74	2.18	2.10	3.58
Mouse 3	1.82	2.89	3.29	1.48	1.84	0.98	0.43
Mean	1.54±0.25	5.30±2.1	1.97±1.5	1.60±0.12	1.77±0.45	1.60±0.57	3.52±3.06

Table 5: CoV(%) of LV function parameters for each investigated mouse over the 3 time points at baseline with RT2 protocol. RT2: $G47$=15, Δt=31.5ms.

	CoV(EDV)	CoV(ESV)	CoV (SV)	CoV (EF)	CoV(LVMED)	CoV(LVMES)	CoV(CO)
Mouse 1	1.27	6.10	2.11	1.54	0.32	2.42	6.35
Mouse 2	2.03	7.46	0.51	1.74	0.99	1.58	4.09
Mouse 3	1.91	2.26	3.16	1.32	1.31	0.31	0.22
Mean	1.74±0.41	5.28±2.70	1.93±1.33	1.54±0.21	0.87±0.50	1.44±1.06	3.55±3.10

Table 6: CoV(%) of LV function parameters for each investigated mouse over the 3 time points at baseline with RT3 protocol. RT3: $G57$=23, Δt=48.3ms.

	CoV(EDV)	CoV(ESV)	CoV (SV)	CoV (EF)	CoV(LVMED)	CoV(LVMES)	CoV(CO)
Mouse 1	2.92	4.72	2.69	0.68	0.25	2.96	4.71
Mouse 2	0.93	6.87	1.70	2.03	0.94	1.15	1.90
Mouse 3	2.28	1.56	3.08	0.93	1.00	1.15	0.75
Mean	2.04±1.02	4.38±2.67	2.49±0.71	1.22±0.72	0.73±0.42	1.74±1.05	2.46±2.04

Table 7: CoV(%) of LV function parameters for each investigated mouse over the 3 time points at stress with RT1 protocol. RT1: $G37$=8, Δt=16.8ms.

	CoV(EDV)	CoV(ESV)	CoV (SV)	CoV (EF)	CoV(LVMED)	CoV(LVMES)	CoV(CO)
Mouse 1	0.60	4.65	0.16	0.44	1.55	1.58	3.72
Mouse 2	2.69	11.55	1.95	1.09	2.79	0.49	10.14
Mouse 3	2.75	7.43	3.42	1.03	0.66	1.48	4.53
Mean	2.01±1.22	7.87±3.47	1.84±1.63	0.85±0.36	1.67±1.07	1.18±0.60	6.13±3.50

Table 8: CoV(%) of LV function parameters for each investigated mouse over the 3 time points at stress with RT2 protocol. RT2: $G_4^7 = 15, \Delta t = 31.5ms$.

	CoV(EDV)	CoV(ESV)	CoV (SV)	CoV (EF)	CoV(LVMED)	CoV(LVMES)	CoV(CO)
Mouse 1	2.27	7.45	1.69	0.59	1.30	1.44	2.15
Mouse 2	2.97	9.91	2.11	0.91	1.56	2.42	10.82
Mouse 3	2.85	7.06	3.27	0.97	4.13	4.56	4.43
Mean	2.7±0.37	8.14±1.54	2.36±0.82	0.82±0.20	2.33±1.56	2.81±1.60	5.80±4.49

Table 9: CoV(%) of LV function parameters for each investigated mouse over the 3 time points at stress with RT3 protocol. RT3: $G57$=23, Δt=48.3ms.

	CoV(EDV)	CoV(ESV)	CoV (SV)	CoV (EF)	CoV(LVMED)	CoV(LVMES)	CoV(CO)
Mouse 1	1.96	1.67	2.37	0.41	0.96	0.56	1.46
Mouse 2	2.72	5.74	2.73	0.64	3.22	1.92	11.38
Mouse 3	1.71	6.95	2.77	1.07	1.28	1.59	4.41
Mean	2.13±0.53	4.79±2.76	2.62±0.22	0.71±0.33	1.82±1.22	1.35±0.71	5.75±5.10

8 Acknowledgments

The acknowledgments have been removed due to data privacy protection.

9 Curriculum Vitae

The curriculum vitae has been removed due to data privacy protection.